

Quantitative Magnetic Resonance Imaging by Nonlinear Inversion of the Bloch Equations

Nick Scholand^{*1,3}, Xiaoqing Wang^{1,3}, Volkert Roeloffs², Sebastian
Rosenzweig^{2,3}, and Martin Uecker^{1,2,3,4}

¹Institute of Biomedical Imaging, Graz University of Technology,
Graz, Austria

²Institute for Diagnostic and Interventional Radiology, University
Medical Center Göttingen, Göttingen, Germany

³German Centre for Cardiovascular Research (DZHK), Partner
Site Göttingen, Göttingen, Germany

⁴Cluster of Excellence “Multiscale Bioimaging: from Molecular
Machines to Networks of Excitable Cells” (MBExC), University of
Göttingen, Göttingen, Germany

February 20, 2023

Submitted to Magnetic Resonance in Medicine

Abstract

Purpose: Development of a generic model-based reconstruction framework for multi-parametric quantitative MRI that can be used with data from different pulse sequences.

Methods: Generic nonlinear model-based reconstruction for quantitative MRI estimates parametric maps directly from the acquired k-space by numerical optimization. This requires numerically accurate and efficient methods to solve the Bloch equations and their partial derivatives. In this work, we combine direct sensitivity analysis and pre-computed state-transition matrices into a generic framework for calibrationless model-based reconstruction that can be applied to different pulse sequences. As a proof-of-concept, the method is implemented and validated for quantitative T_1 and T_2 mapping with single-shot inversion-recovery (IR) FLASH and IR bSSFP sequences in simulations, phantoms, and the human brain.

Results: The direct sensitivity analysis enables a highly accurate and numerically stable calculation of the derivatives. The state-transition matrices efficiently exploit repeating patterns in pulse sequences, speeding

*Nick Scholand, Institute of Biomedical Imaging, Graz University of Technology, Stremayr-
gasse 16/III, 8010 Graz, Austria. scholand@tugraz.at

up the calculation by a factor of 10 for the examples considered in this work, while preserving the accuracy of native ODE solvers. The generic model-based method reproduces quantitative results of previous model-based reconstructions based on the known analytical solutions for radial IR FLASH. For IR bSFFP it produces accurate T_1 and T_2 maps for the NIST phantom in numerical simulations and experiments. Feasibility is also shown for human brain, although results are affected by magnetization transfer effects.

Conclusion: By developing efficient tools for numerical optimizations using the Bloch equations as forward model, this work enables generic model-based reconstruction for quantitative MRI.

Keywords: model-based reconstruction, sensitivity analysis, state-transition matrix, nonlinear inversion, Bloch equations, quantitative MRI

1 Introduction

Conventional quantitative magnetic resonance imaging is based on a two-step process, where first intermediate images are reconstructed and then physical models are fitted pixel-wisely to obtain parameter maps. Acquiring a sufficient amount of high quality images with carefully designed contrasts is required for achieving a good fit. For this reasons, these methods are too slow for many clinical applications. In contrast, nonlinear model-based reconstruction methods formulate image reconstruction as a single inverse problem. They exploit a physical model of the measurement process and directly estimate quantitative parameter maps from k-space. Thus, they make optimal use of the available data and enable highly efficient parameter mapping from signals acquired with sequences that make use of transient magnetization dynamics [1, 2, 3, 4, 5]. These techniques have two problems: They are computationally demanding and they need to be specially designed for each application.

Alternatively, fingerprinting [6] uses a lookup dictionary obtained by Bloch simulations to map the pixels of intermediate images computed directly from undersampled data to quantitative parameter maps. This enables multi-parametric mapping with high acceleration in a flexible and computationally efficient framework, but is not optimal due to its lack of a least-squares data consistency term. Subspace models can be exploited for a more efficient mapping by approximating the physical signal with a larger linear subspace. They reduce the computational demand of the reconstruction very efficiently [7, 8, 9, 10, 11], but are still not optimal because a linear subspace is used to approximate the manifold of possible signals. For complicated spin dynamics a larger number of subspace coefficients may be needed to accurately represent the signal, rendering subspace methods less efficient [5].

The aim of this work is to develop a generic framework for nonlinear model-based reconstruction with accurate signal models for different MRI sequences even with complicated spin dynamics. The generalization of the forward model then allows the use of optimized sequences for which no analytical expression

for their signal can be derived. Fundamentally, such a generic method requires efficient techniques to compute the partial derivatives of the Bloch equations. So far, two different methods were used in MRI. First, symbolic derivatives can be calculated for analytical solutions of the Bloch equations for special sequences [12, 13, 14] and this can be generalized to chains of small blocks using automatic differentiation [15, 16]. These methods require idealized assumptions such as hard pulse approximation and perfect inversion. In more complicated scenarios with long pulses or imperfect inversion they require high discretization rates or suffer from errors. Second, derivatives can be estimated using difference quotients [17, 18]. This method fully exploits the generality of full Bloch simulations, but is computationally expensive and requires careful tuning to balance accuracy and noise amplification.

To overcome these limitations, this work uses a direct sensitivity analysis [19] to compute the derivatives of the Bloch equations for arbitrary sequences with high accuracy by solving an extended system of ordinary differential equations (ODE). The technique is validated using an analytical model of an IR bSSFP sequence and is compared to results obtained from difference quotients methods. To further improve computation speed, pre-computed state-transition matrices are applied to arbitrary initial conditions solving the required ODEs for all repeating parts of an MRI sequence efficiently. They are validated by comparing them to the direct application of a Runge-Kutta ODE solver. We further integrate both techniques in a nonlinear model-based reconstruction with integrated calibration-less parallel imaging. For IR FLASH, we show that the methods reproduce the results of an analytical model. In a numerical and measured phantom study with an IR bSSFP sequence we refine the flexible forward model of the generic model-based reconstruction to include realistic simulations with slice-selective excitations and hyperbolic secant inversion pulses. Thus, we show that the reconstruction quality benefits much from the more physically accurate modelling leading to accurate T_1 and T_2 parameter maps. Finally, we test the developed technique on in-vivo brain data from a healthy volunteer.

Parts of this work have been published in [20, 21, 22, 23].

2 Theory

In the following, we briefly explain the concepts of a direct sensitivity analysis and its application to the Bloch equations (SAB). We then describe how state-transition matrices (STMs) can be used to accelerate the solution of the ODEs. Afterwards, both methods are integrated into a nonlinear model-based reconstruction method.

2.1 Sensitivity Analysis of the Bloch Equations

We consider the temporal evolution of a magnetization vector $\mathbf{M}(\mathbf{c}, t)$ depending on a vector of parameters \mathbf{c} and time t . The temporal behaviour of its

components $M_i(\mathbf{c}, t)$ is described by the Bloch equations as a system of ODEs

$$\frac{d}{dt}M_i(\mathbf{c}, t) = f_i(\mathbf{M}(\mathbf{c}, t), \mathbf{c}, t), \quad (1)$$

where f defines the dynamics. The partial derivative of the component M_i with respect to the parameter c_j defines the (i, j) -th entry

$$Z_{ij}(t) = \frac{\partial M_i(\mathbf{c}, t)}{\partial c_j} \quad (2)$$

of the sensitivity matrix $\mathbf{Z}(t)$.

Using direct sensitivity analysis [19] one obtains $\mathbf{Z}(t)$ by solving an additional set of ODEs. Assuming that the partial and ordinary derivatives interchange, the time derivative of the (i, j) -th entry of \mathbf{Z} is

$$\frac{d}{dt}Z_{ij}(t) = \frac{d}{dt} \left(\frac{\partial M_i(\mathbf{c}, t)}{\partial c_j} \right) = \frac{\partial}{\partial c_j} \left(\frac{dM_i(\mathbf{c}, t)}{dt} \right). \quad (3)$$

Substituting $\frac{dM_i(\mathbf{c}, t)}{dt}$ then yields

$$\frac{d}{dt}Z_{ij}(t) = \frac{\partial}{\partial c_j} f_i(\mathbf{M}(\mathbf{c}, t), \mathbf{c}, t). \quad (4)$$

With the chain rule, the resulting ODE becomes

$$\begin{aligned} \frac{d}{dt}Z_{ij}(t) &= \frac{\partial f_i(\mathbf{M}(\mathbf{c}, t), t, \mathbf{c})}{\partial c_j} + \sum_j \frac{\partial f_i(\mathbf{M}(\mathbf{c}, t), \mathbf{c}, t)}{\partial M_j} \frac{\partial M_j(\mathbf{c}, t)}{\partial c_j} \\ &= \frac{\partial f_i(\mathbf{M}(\mathbf{c}, t), \mathbf{c}, t)}{\partial c_j} + \sum_j \frac{\partial f_i(\mathbf{M}(\mathbf{c}, t), \mathbf{c}, t)}{\partial M_j} Z_{ij}, \end{aligned} \quad (5)$$

where $\frac{\partial f_i(\mathbf{M}(\mathbf{c}, t), \mathbf{c}, t)}{\partial M_j}$ describes the (i, j) -th element of the Jacobian $J_{i,j}$. This can be written compactly for the sensitivity matrix $\mathbf{Z}(t)$ as

$$\frac{d}{dt}\mathbf{Z}(t) = \mathbf{f}_c(\mathbf{M}(\mathbf{c}, t), \mathbf{c}, t) + \mathbf{J}(\mathbf{M}(\mathbf{c}, t), \mathbf{c}, t) \cdot \mathbf{Z}(t). \quad (6)$$

If a direct sensitivity analysis is applied to the Bloch equations for the parameters R_1 , R_2 and B_1 , the ODE in Eqs. 6 describing the temporal evolution of the sensitivities becomes

$$\frac{d}{dt}\mathbf{Z} = \begin{pmatrix} 0 & -M_x & -\gamma \sin \phi M_z \\ 0 & -M_y & \gamma \cos \phi M_z \\ M_0 - M_z & 0 & \gamma(\sin \phi M_x - \cos \phi M_y) \end{pmatrix} + \begin{pmatrix} -R_2 & \gamma B_z & -\gamma \sin \phi B_1 \\ -\gamma B_z & -R_2 & \gamma \cos \phi B_1 \\ \gamma \sin \phi B_1 & -\gamma \cos \phi B_1 & -R_1 \end{pmatrix} \cdot \mathbf{Z}. \quad (7)$$

depending on the x , y and z components of the magnetization \mathbf{M} , the magnetic fields B_z and B_1 as well as the RF pulse phase ϕ . Eq. 7 is solved jointly with the Bloch Eqs. 1 which provide the time-dependent solutions for M_x , M_y , and M_z .

2.2 State-Transition Matrices

By embedding the magnetization vector into a four-dimensional space

$$\mathbf{M}(\mathbf{c}, t) = \begin{pmatrix} M_x(\mathbf{c}, t) \\ M_y(\mathbf{c}, t) \\ M_z(\mathbf{c}, t) \\ 1 \end{pmatrix}, \quad (8)$$

we obtain a formulation of the Bloch Eqs. 1 as a system of homogeneous ODEs

$$\frac{d\mathbf{M}(\mathbf{c}, t)}{dt} = \mathbf{f}(\mathbf{M}(\mathbf{c}, t), \mathbf{c}, t) = \mathbf{A}(\mathbf{c}, t) \mathbf{M}(\mathbf{c}, t), \quad (9)$$

with the system matrix

$$\mathbf{A}(\mathbf{c}, t) = \begin{pmatrix} -R_2 & \gamma \mathbf{G}_z(t) \cdot \mathbf{r} & -\gamma B_y(t) & 0 \\ -\gamma \mathbf{G}_z(t) \cdot \mathbf{r} & -R_2 & \gamma B_x(t) & 0 \\ \gamma B_y(t) & -\gamma B_x(t) & -R_1 & M_0 R_1 \\ 0 & 0 & 0 & 0 \end{pmatrix}, \quad (10)$$

at location \mathbf{r} depending on time t , the z -gradient \mathbf{G}_z and the magnetic fields $B_{x,y}$.

The Bloch equations can be solved directly for time-dependent coefficients $\mathbf{A}(t)$ using standard ODE solvers. Here we describe the pre-computation of STMs as more efficient way to solve the equations for MRI sequences with repeating patterns. A STM $\mathbf{S}_{t_1 \rightarrow t_2}$ describes the evolution of an arbitrary starting magnetization $\mathbf{M}(\mathbf{c}, t_1)$ for the time span from t_1 to t_2 including all effects from relaxation and time-dependent external RF fields. This compresses the temporal evolution to a single matrix multiplication

$$\mathbf{M}(\mathbf{c}, t_2) = \mathbf{S}_{t_1 \rightarrow t_2} \mathbf{M}(\mathbf{c}, t_1). \quad (11)$$

The computation of $\mathbf{S}_{t_1 \rightarrow t_2}$ is based on derivation of Eq. 11

$$\frac{d\mathbf{M}(\mathbf{c}, t_2)}{dt_2} = \frac{d}{dt_2} (\mathbf{S}_{t_1 \rightarrow t_2} \mathbf{M}(\mathbf{c}, t_1)). \quad (12)$$

Using the Bloch Eqs. 9 to replace the time derivative on the left side and using $\frac{d\mathbf{M}(t_1)}{dt_2} = 0$ for the right, we obtain

$$\mathbf{A}(t_2) \mathbf{M}(\mathbf{c}, t_2) = \left(\frac{d}{dt_2} \mathbf{S}_{t_1 \rightarrow t_2} \right) \mathbf{M}(\mathbf{c}, t_1). \quad (13)$$

By using Eqs. 11 and switching both sides we obtain

$$\frac{d}{dt_2} \mathbf{S}_{t_1 \rightarrow t_2} \mathbf{M}(\mathbf{c}, t_1) = \mathbf{A}(t_2) \mathbf{S}_{t_1 \rightarrow t_2} \mathbf{M}(\mathbf{c}, t_1). \quad (14)$$

As this holds for arbitrary $\mathbf{M}(\mathbf{c}, t_1)$ and by renaming t_2 as t a system of ODEs

$$\frac{d}{dt} \mathbf{S}_{t_1 \rightarrow t} = \mathbf{A}(t) \mathbf{S}_{t_1 \rightarrow t} \quad (15)$$

for the entries of the STM is derived. This ODEs 15 can be solved for estimating $\mathbf{S}_{t_1 \rightarrow t_2}$ column-wisely with an ODE solver [24, 25] with initial conditions

$$\mathbf{S}_{t_1 \rightarrow t_1} = \mathbf{1} . \quad (16)$$

The solution of the state-transition ODE in Eqs. 15 can be formally defined as a time ordered exponential

$$\mathbf{S}_{t_1 \rightarrow t_2} = \prod_{t_1}^{t_2} e^{\mathbf{A}(\tau)d\tau} \equiv \mathcal{T} \left\{ e^{\int_{t_1}^{t_2} \mathbf{A}(\tau)d\tau} \right\} \quad (17)$$

$$\equiv \lim_{N \rightarrow \infty} \left(e^{\mathbf{A}(t_N)\Delta t} e^{\mathbf{A}(t_{N-1})\Delta t} \dots e^{\mathbf{A}(t_1)\Delta t} e^{\mathbf{A}(t_0)\Delta t} \right) . \quad (18)$$

This links the proposed technique to approximation methods based on matrix-exponentials computed using discretized sampling [26, 27].

This technique is not limited to the Bloch Equations, but can be extended to also include the sensitivity analysis for the three partial derivatives R_1 , R_2 and B_1 . This is further described in Appendix A.

2.3 Bloch Model-Based Reconstruction

In the following, we integrate the generic Bloch operator \mathcal{B} into a nonlinear model-based reconstruction framework with non-Cartesian, calibrationsless, parallel imaging and compressed sensing as illustrated in Figure 1. The reconstruction method solves the nonlinear inverse problem for the maps $\mathbf{x} = (\mathbf{x}_p \ \mathbf{x}_c)^T$ with the physical parameters $\mathbf{x}_p = (R_1 \ R_2 \ M_0 \ B_1)^T$ and coil sensitivities $\mathbf{x}_c = (c_1 \ \dots \ c_N)^T$ by optimizing

$$\hat{\mathbf{x}} = \underset{\mathbf{x}}{\operatorname{argmin}} \|\mathbf{y} - \mathcal{A}(\mathbf{x})\|_2^2 + \alpha \mathbf{Q}(\mathbf{x}_c) + \beta \mathbf{R}(\mathbf{x}_p) . \quad (19)$$

Eq. 19 includes the forward-operator \mathcal{A} , the measured data \mathbf{y} , the Sobolev norm \mathbf{Q} with its regularization parameter α to enforce the smoothness of coil profiles [28] and B_1 maps. A joint sparsity constraint \mathbf{R} is applied to the other parameter maps [29, 30]. The full forward operator is $\mathcal{A} = \mathcal{PFCB}$. It is solved by the Iteratively Regularized Gauss-Newton Method (IRGNM)

$$\begin{aligned} \hat{\mathbf{x}}_{n+1} = \underset{\mathbf{x}}{\operatorname{argmin}} & \|D\mathcal{A}(\mathbf{x}_n)(\mathbf{x} - \mathbf{x}_n) + \mathcal{A}(\mathbf{x}_n) - \mathbf{y}\|_2^2 \\ & + \alpha_n \mathbf{Q}(\mathbf{x}_c) + \beta_n \mathbf{R}(\mathbf{x}_p) \end{aligned} \quad (20)$$

with the Jacobian $D\mathcal{A}(\mathbf{x}_n)$ and the regularization parameters $\alpha_n = \alpha_0 \cdot q^n$ and $\beta_n = \beta_0 \cdot q^n$ at the n th iteration step. Here, \mathcal{C} is the nonlinear parallel imaging operator combining the signal with the coil profiles, \mathcal{F} represents the Fourier operator, \mathcal{P} the sampling pattern. The generic operator \mathcal{B} takes information about the applied sequence and outputs the simulated signal based on the STM technique. The partial derivatives of \mathcal{B} are calculated using the direct sensitivity analysis. The derivatives of \mathcal{A} are described in Appendix B.

3 Methods

3.1 Implementation

All simulations and reconstructions are implemented in the Berkeley Advanced Reconstruction Toolbox (BART) using single-precision floating point arithmetic [31]. The Bloch operator \mathcal{B} is implemented in BARTs nonlinear operator framework [32]. The calibrationless model-based reconstruction is based on an IRGNM-FISTA following Wang *et al.* [13] and we refer to this work for further details. The Bloch operator includes a pixel-wise calculation of the signal evolution using STMs (Section 2.2) and of the partial derivatives with SAB (Section 2.1). ODEs are solved using the a Runge-Kutta algorithm (RK54) with adaptive step-sizes. The error tolerances are chosen to be 10^{-7} for the simulation comparisons in Section 2.1 and 2.2 as well as 10^{-6} for further reduced computational costs in the Bloch model-based reconstructions. The Runge-Kutta solver exploits weights published by Dormand and Prince [33]. For balancing the relative scaling of the partial derivatives during the optimization of Eq. 19 pre-conditioning following Wang *et al.* [13] is used. The initial wavelet regularization is set to $\alpha_0=\beta_0=1$ and decreased by $q=1/2$ in each Newton iteration. The output of the Bloch model operator \mathcal{B} is scaled according to Section D. As a globalized Newton method, the IRGNM does not require fine tuning of initial values. Here, the maps are initialized with the constants $R_1 = 1$ Hz, $R_2 = 1$ Hz, $M_0 = 1$, $B_1 = 0$ and the coil profiles are initialized with zero.

For comparison, we also implemented the reparameterized Look-Locker model from equation 29 in the same model-based reconstruction framework following Wang *et al.* [13].

3.2 Validation of Bloch Simulation

The accuracy of the SAB technique is validated with an IR bSSFP sequence for tissue with $T_1/T_2 = 1250/45$ ms. An analytical solution for the IR bSSFP signal can be derived from the Bloch equations [34] assuming hard pulses, a perfect inversion and a perfect non-selective excitation. The symbolic partial derivatives with respect to the parameters R_1 , R_2 , M_0 and B_1 are calculated in Appendix F and are used as ground truth. For validation of the derivatives the ODE simulation parameters are chosen to be close to the assumptions of the analytical model. The ODE solution for the derivatives is also compared to the difference quotient techniques (DQ) calculated using two simulations $M_{t,p}$ and $M_{t,p+h}$ differing by a small perturbation h for all parameters $p \in (T_1, T_2, M_0, B_1)$ and time points t :

$$\frac{\partial M_t}{\partial p} = \frac{M_{t,p+h} - M_{t,p}}{h} \quad (21)$$

The size of the perturbation is decreased until numerical noise dominates.

To validate the STM approach in the presence of RF pulses, gradients, and relaxation, a slice-selective excitation of a Hamming-windowed sinc-shaped inversion pulse with $T_{RF} = 1$ ms, BWTP=1, $\Delta z = 10$ mm, $G_z = 10$ mT/m is

simulated. Relaxation parameters are selected based on typical human white matter values at 3 T: $T_1/T_2 = 832/80$ ms [35]. The STM simulation is computed with the Runge-Kutta solver and the magnetization just before the slice rewriter is compared to a direct simulation exploiting the same solver. For comparison a traditional Bloch simulation technique based on temporal discretization with rotational matrices (ROT) is performed using a discretization rate of 1 MHz. According to the analysis shown in Figure S3, a sampling rate of 1 MHz is required for ROT to accurately model complex spin dynamics that include slice-selective RF pulses.

The simulation speed is analyzed for a FLASH sequence with $FA=8^\circ$, $TR/TE=3.1/1.7$ ms and $T_{RF}=1$ ms simulated for 101 isochromats homogeneously distributed along a slice of 0.02 m width and using a slice-selection gradient of 12 mT/m. The tissue parameters are set to relaxation times of white matter at 3 T. The simulations were executed on a single Intel(R) i7-8565U CPU core at 1.80 GHz.

3.3 Validation of Reconstruction

To validate the model-based reconstruction we further perform validations on numerical and experimental phantoms as well as in vivo data for both single-shot IR FLASH and IR bSSFP sequences with tiny golden-angle based radial sampling. The IR bSSFP sequence includes a prior $\alpha/2$ -TR/2 pulse to achieve a smooth signal evolution during the transient state [36, 37]. To be able to decouple the information of T_1 and T_2 for an IR bSSFP sequence (see section E) a B_1 map is acquired on the same slice using a vendor protocol based on rapid B_1 estimation with preconditioned RF pulses and Turbo-FLASH readout [38]. All sequence parameters are shown in Table 1.

Phantom data for an IR FLASH sequence published by Wang et al. [39] was downloaded from Zenodo [40]. This data was measured on a 3 T Magnetom Skyra by Siemens Healthcare (Erlangen, Germany) with a 20 channel head-coil. The measured phantom is a commercial reference phantom (Diagnostic Sonar LTD, Scotland, UK, Eurospin II, gel 3, 4, 7, 10, 14, and 16) consisting of six tubes with known T_1 relaxation values surrounded by water. A digital phantom of the dataset is created with the same sequence and acquisition characteristics as the downloaded measurement. The relaxation parameters were set to the estimated reference T_1 and T_2 values from previous studies [13, 41]. Additional phantom data for a radial single-shot IR bSSFP sequence was acquired on the T_2 spheres of a NIST phantom [42] on the same scanner and the same 20 channel head-coil. For comparison gold-standard maps of T_1 and T_2 are estimated on the same slice of the NIST phantom using fully-sampled single-echo spin-echo sequences. All phantom measurements were performed at constant room temperature ($\sim 21^\circ\text{C}$). The estimated quantitative values from gold-standard scans were used to simulate a second digital phantom with the same geometry as the measured T_2 -spheres of the NIST geometry (model 130).

Radial single-shot IR FLASH and IR bSSFP data for a brain of a healthy volunteer was acquired with a 20 channel head-coil on a Siemens Skyra 3T system (Siemens Healthcare, Erlangen, Germany) after obtaining written informed

consent. The IR FLASH data was measured with a TR/TE of 4.1/2.58 ms, a flip angle of 6° , a band-width-time-product (BWTP) of 4 and a RF pulse duration of 1 ms. The field-of-view (FOV) was $220 \times 220 \text{ mm}^2$ measured at 512 samples with two-fold oversampling. The single-shot IR bSSFP data was acquired with two different pulse durations: 1 ms and 2.5 ms respectively. The repetition and echo times were set to 4.88/2.44 ms and 10.8/5.4 ms. A FOV of $200 \times 200 \text{ mm}^2$, a flip angle of 45° , a BWTP of 4 and a base resolution of 256 was chosen and the same for both measurements.

The phantom and in vivo IR FLASH datasets are reconstructed with both the Look-Locker model and the Bloch model-based technique. As the IR FLASH sequence is insensitive to R_2 , its estimation in the Bloch model-based reconstruction was turned off by setting the scaling in the pre-conditioner to zero. The initial free decay of 15.3 ms during the non-selective hyperbolic secant inversion pulse is corrected in both cases using the correction published by Deichmann et al. [43].

The flexibility of the Bloch model-based reconstruction with its ability to also model more complex sequences is demonstrated using single-shot IR bSSFP. In the analysis of the measured dataset the B_1 map is used in the forward model for scaling the nominal flip angle for each pixel. Additionally, the B_1 estimation is turned off by setting the scaling to zero in the pre-conditioning.

The method is numerically validated using a digital phantom of the T_2 sphere of the NIST phantom (model version 130) implemented in BART. The multi-coil phantom is simulated in the frequency domain with the same sequence parameters as the measurement. The eight coils are compressed to four virtual coils using a singular-value decomposition (SVD). Complex Gaussian noise is added before coil compression to further avoid an inverse crime. To ensure realistic physical conditions the simulated signal model includes a non-selective hyperbolic secant inversion pulse and slice-selective excitations using multiple isochromats distributed over equally spaced slice-selection gradient positions. While analytical solutions of the Bloch equations require the assumption of perfect inversions and ideal non-selective excitation, the generic simulation of the Bloch model-based reconstruction technique can simulate more realistic signal models. We show how step-wise improvements to the model allow more accurate modelling of actual measurements. This is demonstrated on the numerical and measured NIST phantom datasets by performing reconstructions with various different assumptions about the signal model. The first reconstruction uses a model close to the analytical formula by assuming a perfect inversion and a non-selective excitation. We then add a realistic slice-selective excitation simulated as mean signal of various homogeneously spaced isochromats along the slice-selection gradient. To also model the effect of non-optimal inversion efficiency, the final reconstruction includes an extended model with realistic non-selective hyperbolic secant inversion.

The radial single-shot IR bSSFP in vivo data is reconstructed using the most realistic model. For comparison, the single-shot IR FLASH measurement was acquired on the same slice and reconstructed with the Bloch model-based reconstruction assuming a realistic IR FLASH signal model with non-selective

hyperbolic secant inversion and gradient based slice-selective excitation model to estimate a T_1 map.

Details about the measurements can be found in Table 1.

4 Results

4.1 Validation of Bloch Simulation

Figure 2 shows the partial derivatives for an IR bSSFP sequence with respect to R_1 , R_2 and B_1 for the analytical reference, the SAB technique and difference quotient (DQ) techniques with different perturbations h on the left. On the right Figure 2 presents the differences of DQ and SAB to the analytical reference.

As expected, the error of DQ decreases for small perturbations until numerical noise starts to dominate for very small h .

The SAB technique demonstrates a high accuracy and precision of estimating partial derivatives without requiring tuning of the perturbation level.

Figure 3.A compares the simulation results of a Hamming-windowed sinc-shaped inversion pulse using the Runge-Kutta 54 method with Dormand-Prince weights (RK54) [33], STM, and ROT technique.

The error of the STM simulation is dominated by numerical noise due to limited floating point precision. With the parameters used here, the STM technique has substantially lower point-wise errors than ROT.

It demonstrates that STM reproduces the RK54 technique for finding solutions to the Bloch equations extremely well, while ROT is affected by errors due to the discretization with fixed sampling rate and its nature of being a first order method constrained to single floating point precision here. The runtime of RK54, STM and ROT is shown in Figure 3.B. The computational cost of ROT increases linear with higher sampling rates. The STM has higher initial costs than the other techniques which reflect the initial calculation of the state-transition matrices. The other methods are therefore faster for a small number of repetitions. For more repetitions, the STM becomes much faster as it requires only a few matrix multiplications per TR. A detailed comparison of the computational cost and accuracy of the RK54, STM and ROT techniques for various error tolerances and sampling rates can be found in Supplementary Section S3 and Supplementary Figure S3.

4.2 Validation of Reconstruction

The Bloch model-based reconstruction was compared to the Look-Locker model-based version for simulated (Figure 4.A) and measured single-shot IR FLASH phantom data (Figure 4.B). Both methods recover high quality T_1 maps with small differences. Values for the same Regions-of-Interests (ROIs) are very simi-

lar leading to their position on the diagonal of the Bloch vs. Look-Locker plot on the most right of Figure 4.A and Figure 4.B. The reconstructed tubes are very homogeneous in both reconstructions leading to low standard deviations. Reconstructions using different regularization parameters or no regularization are shown in Supplementary Figure S4 and Supplementary Figure S6, respectively.

In the difference map between the T_1 maps of the two methods only the water background shows areas with minor differences. This probably results from small differences in the Sobolev regularization on the flip angle map in both techniques. At the walls of the inner tubes there is not enough signal and the T_1 maps are not well defined. Results for the radial single-shot in vivo IR FLASH data are shown in Figure 4.C. The parameter maps are visually indistinguishable except for minor artifacts in the areas of the head with flow related effects, which are not modelled by both signal models. The T_1 values in the marked ROIs for representative white and gray matter areas show a very good correspondence. The homogeneity within the white matter is high corresponding to a small standard deviation.

The complex M_0 parameter map in Figure 4.D reconstructed with the Bloch model-based reconstruction is of good quality showing no artifacts and a homogeneous phase. Only in border regions phase changes are present which are most likely caused by fat. The relative flip angle map is globally lower than one. It combines the effect of an imperfect slice-selective excitation and the present B_1 field. The intensity and phase of the estimated SVD-compressed virtual coil sensitivities is comparable to intensity and phase of sensitivities estimated with ESPiRiT [44](results not shown).

Figure 5 shows the reconstructed T_1 and T_2 maps of the digital NIST phantom (5.A) and the measurement (5.B) using the radial single-shot IR bSSFP acquisition for different models compared to the reference values in Bland-Altman plots. The most simplistic model assumes a perfect inversion and an ideal non-selective excitation (**Perfect Inversion**) and shows inaccuracies in the T_1 and T_2 estimation. By integrating a slice-selective excitation (**Slice**) the errors in T_2 are significantly reduced leaving an offset in T_1 . Adding a realistic hyperbolic secant inversion pulse to the forward model (**Pulse+Slice**) corrects for the T_1 offset leading to an accurate estimation of the relaxation parameters. These effects are present in both: the simulation and the measured data reconstructions. Important to note is that the NIST phantoms contains some spheres with extreme T_1 and T_2 parameters [42], which were excluded from the Bland-Altman analysis in Figure 5.A and 5.B for improved visualization. In particular, the three highest T_2 values (1.450 s, 0.388 s and 0.271 s) were removed for the reconstruction from simulated data and the highest and lowest T_2 values (1.450 s, 0.006 s) for the measured data. Especially the simple model has difficulties in finding the correct relaxation parameters in the reconstruction of the measured data, so that the mean value is outside the plotted region. A direct comparison of reference and estimated parameters in a diagonal plot can be found in Supplementary Figure S1. A Bland-Altman plot with all data points is shown in Supplementary Figure S2.

Reconstructed T_1 and T_2 parameter maps for the two single-shot IR bSSFP

scans of a human brain are shown in Figure 6. For comparison, a map with the Look-Locker model-based reconstruction of the IR FLASH scan of the same slice is added. Both IR bSSFP reconstructions show large offsets in T_1 compared to the IR FLASH reference. The relaxation values for the two analyzed ROIs are listed in Table 2. The differences are smaller for the longer TR and longer RF pulse duration T_{RF} compared to the short pulse protocol. This is likely due to the magnetization transfer effect (MT) that affects the IR bSSFP sequence but is not included in the current study.

The reconstruction times depend on the complexity of the forward model. The reconstruction of the IR FLASH datasets took about 80 s on a AMD EPYC 7662 64-Core CPU and a Nvidia A100-SXM-80GB GPU. The reconstruction of the simple forward model of the IR bSSFP NIST phantom dataset took 60 s, while the most complex model reconstruction took 38 min. The longest reconstruction times were required for the in vivo IR bSSFP dataset with short RF pulse. The strong slice-selection gradient prolonged the reconstruction to about 75 min.

5 Discussion

A nonlinear model-based reconstruction framework can be used in combination with well-crafted sequences and their analytical signal representations to accelerate quantitative MRI. This work presents a generalization of this well-known approach to arbitrary MRI sequences by exploiting the Bloch equations directly as forward model. This method becomes computationally feasible by including a direct sensitivity analysis of the Bloch equations. It allows us to use a generic ODE solver to compute the derivatives required by efficient nonlinear optimization algorithms such as the IRGNM. In comparison to techniques based on difference quotients it produces highly stable and accurate partial derivatives without the need of fine tuning perturbation levels. This was shown by estimating partial derivatives of an IR bSSFP experiment with the mentioned techniques and by comparing their results to the underlying analytical reference.

To further reduce computational demand, we exploit pre-computed STMs. They are used to solve the Bloch equations and the system describing their sensitivities simultaneously for arbitrary initial conditions for a given time span. They reduce the spin dynamics even in the presence of external fields, gradients, and relaxation to single matrix multiplications. It dramatically speeds up the reconstruction whenever the MRI sequence contains repeated patterns as it is often the case. In the presented example of the FLASH sequence with 101 isochromats along a slice and simulated for 1000 repetitions, the run-time of the simulation was reduced by a factor of 10 from 5 s down to 0.5 s in comparison to a regular Runge-Kutta ODE solver. Even in the presence of gradients, RF pulses and relaxation the slice-profile analysis showed the high accuracy of the STM technique in reproducing the ODE solver results.

Experimentally we confirmed that the Bloch model-based reconstruction reproduces the Look-Locker model as a special case. A comparison between both

techniques showed only minor differences in the T_1 maps reconstructed from the single-shot phantoms and single-shot in vivo data.

The integration of a generic Bloch simulation into the reconstruction adds the flexibility to analyze a broad variety of sequences. As an initial example, we applied the technique to IR bSSFP sequence and validated it using a numerical and measured NIST phantom dataset. By correctly modelling the slice-selective excitation and a non-selective hyperbolic secant inversion pulse highly accurate T_1 and T_2 maps could be obtained.

For a human brain, T_1 maps estimated from an IR bSSFP sequence were compared to Bloch model-based reconstructions of an IR FLASH acquisition of the same slice both including non-selective hyperbolic inversion and a slice-selective excitation. Here, differences could be observed which are likely caused by MT [45]. This hypothesis is supported by the fact that prolonging the RF pulse duration and increasing the TR reduced the differences, but preliminary results (Supplementary Section S5) suggest that this does not explain the complete discrepancy and that other effects may also play a role. The NIST phantom measurement is not affected by MT effects, because it is based on water [42]. The IR FLASH measurement is assumed to be unaffected by MT because of its small flip angle [46].

At this stage, the most relevant practical limitation is the need to manually tune the scaling factors used for pre-conditioning. For each analyzed sequence the relative scaling between the partial derivatives needs to be balanced manually to ensure smooth convergence. Future work is going to investigate automatic scaling techniques [47, 48].

Further extensions could be the application to hybrid state free precession sequences [26, 49], multi-echo inversion-recovery sequences [50], and magnetization transfer models [27].

6 Conclusion

This work developed a generic framework for model-based reconstruction using the Bloch equations. The approach is validated numerically and tested experimentally using phantom and in-vivo scans.

Acknowledgments

We thank Moritz Blumenthal and Christian Holme for discussions and help with BART.

This project was supported by the DZHK (German Centre for Cardiovascular Research), and funded in part by the Deutsche Forschungsgemeinschaft (DFG, German Research Foundation) under Germany’s Excellence Strategy - EXC 2067/1- 390729940, and funded in part by NIH under grant U24EB029240. We also gratefully acknowledge the support of the NVIDIA corporation with the donation of one NVIDIA TITAN Xp GPU for this research.

Data Availability

The data of this work was uploaded to Zenodo @doi:10.5281/zenodo.6992763. The scripts reproducing all figures of this manuscript are published at Github @mrirecon/bloch-moba.

The reconstruction code is implemented in BART with commit e641e74b.

A tutorial about the usage of the Bloch model-based reconstruction with BART can be found at Github @mrirecon/bloch-tutorial.

Conflict of interest

The authors declare no potential conflict of interests.

References

- [1] Graff C., Li Z., Bilgin A., Altbach M. I., Gmitro A. F., Clarkson E. W.. Iterative T2 estimation from highly undersampled radial fast spin-echo data. *Proc. Int. Soc. Mag. Reson. Med.*. 2006;14:925.
- [2] Olafsson V. T., Noll D. C., Fessler J. A.. Fast Joint Reconstruction of Dynamic R_2^* and Field Maps in Functional MRI. *IEEE Trans. Med. Imag.*. 2008;27(9):1177–1188.
- [3] Block K. T., Uecker M., Frahm J.. Model-Based Iterative Reconstruction for Radial Fast Spin-Echo MRI. *IEEE Trans. Med. Imaging*. 2009;28(11):1759–1769.
- [4] Sumpf T. J., Uecker M., Boretius S., Frahm J.. Model-based nonlinear inverse reconstruction for T2-mapping using highly undersampled spin-echo MRI. *J. Magn. Reson. Imaging*. 2011;34(2):420-428.
- [5] Wang Xiaoqing, Tan Zhengguo, Scholand Nick, Roeloffs Volkert, Uecker Martin. Physics-based Reconstruction Methods for Magnetic Resonance Imaging. *Philos. Trans. R. Soc. A.*. 2021;379(2200).
- [6] Ma D., Gulani V., Seiberlich N., et al. Magnetic resonance fingerprinting. *Nature*. 2013;495(7440):187-192.
- [7] Petzschner Frederike H., Ponce Irene P., Blaimer Martin, Jakob Peter M., Breuer Felix A.. Fast MR parameter mapping using k-t principal component analysis. *Magnetic Resonance in Medicine*. 2011;66(3):706-716.
- [8] Huang Chuan, Graff Christian G, Clarkson Eric W, Bilgin Ali, Altbach Maria I. T2 mapping from highly undersampled data by reconstruction of principal component coefficient maps using compressed sensing. *Magn. Reson. Med.*. 2012;67(5):1355–1366.

- [9] Zhao Bo, Lu Wenmiao, Hitchens T Kevin, Lam Fan, Ho Chien, Liang Zhi-Pei. Accelerated MR parameter mapping with low-rank and sparsity constraints. *Magn. Reson. Med.*. 2015;74(2):489–498.
- [10] Tamir J. I., Uecker M., Chen W., et al. T2 shuffling: Sharp, multicontrast, volumetric fast spin-echo imaging. *Magn. Reson. Med.*. 2017;77(1):180–195.
- [11] Assländer Jakob, Cloos Martijn A, Knoll Florian, Sodickson Daniel K, Hennig Jürgen, Lattanzi Riccardo. Low rank alternating direction method of multipliers reconstruction for MR fingerprinting. *Magnetic resonance in medicine*. 2018;79(1):83–96.
- [12] Hilbert Tom, Sumpf Tilman J., Weiland Elisabeth, et al. Accelerated T2 mapping combining parallel MRI and model-based reconstruction: GRAP-PATINI. *J. Magn. Reson. Imaging*. 2018;48(2):359–368.
- [13] Wang Xiaoqing, Roeloffs Volkert, Klosowski Jakob, et al. Model-based T1 mapping with sparsity constraints using single-shot inversion-recovery radial FLASH. *Magn. Reson. Med.*. 2018;79(2):730–740.
- [14] Tan Zhengguo, Voit Dirk, Kollmeier Jost M., Uecker Martin, Frahm Jens. Dynamic water/fat separation and inhomogeneity mapping adjoint estimation using undersampled triple-echo multi-spoke radial FLASH. *Magn. Reson. Med.*. 2019;82(3):1000–1011.
- [15] Lee Philip K., Watkins Lauren E., Anderson Timothy I., Buonincontri Guido, Hargreaves Brian A.. Flexible and efficient optimization of quantitative sequences using automatic differentiation of Bloch simulations. *Magn. Reson. Med.*. 2019;82(4):1438–1451.
- [16] Dong Guozhi, Hintermüller Michael, Papafitsoros Kostas. Quantitative Magnetic Resonance Imaging: From Fingerprinting to Integrated Physics-Based Models. *SIAM J. Imag. Sci.*. 2019;12(2):927–971.
- [17] Ben-Eliezer Noam, Sodickson Daniel K., Shepherd Timothy, Wiggins Graham C., Block Kai Tobias. Accelerated and motion-robust in vivo T2 mapping from radially undersampled data using bloch-simulation-based iterative reconstruction. *Magn. Reson. Med.*. 2016;75(3):1346–1354.
- [18] Sbrizzi Alessandro, Heide Oscar, Cloos Martijn, et al. Fast quantitative MRI as a nonlinear tomography problem. *Magn Reson Imaging*. 2018;46:56 - 63.
- [19] Dickinson Robert P., Gelinias Robert J.. Sensitivity analysis of ordinary differential equation systems-A direct method. *J. Comput. Phys.*. 1976;21(2):123–143.
- [20] Scholand N., Wang X., Rosenzweig S., Uecker M.. Generalized model-based reconstruction for quantitative MRI using the Bloch-Equations. *Magn. Reson. Mater. Phy.*. 2019;36:32(Suppl 1): 235.

- [21] Scholand N., Wang X., Rosenzweig S., Holme H. C. M., Uecker M.. Generic Quantitative MRI using Model-Based Reconstruction with the Bloch Equations. *Proc. Intl. Soc. Mag. Reson. Med.*. 2020;28.
- [22] Scholand Nick, Graf Christina, Uecker Martin. Efficient Bloch Simulation Based on Precomputed State-Transition Matrices. *Proc. Intl. Soc. Mag. Reson. Med.*. 2022;30.
- [23] Scholand Nick, Uecker Martin. Sensitivity Analysis of the Bloch Equations. *Proc. Intl. Soc. Mag. Reson. Med.*. 2022;30.
- [24] Moler C., Loan C.. Nineteen Dubious Ways to Compute the Exponential of a Matrix. *SIAM Rev.*. 1978;20(4).
- [25] Moler Cleve, Loan Charles Van. Nineteen Dubious Ways to Compute the Exponential of a Matrix, Twenty-Five Years Later*. *SIAM Rev.*. 2003;45(1):3.
- [26] Assländer Jakob, Novikov Dmitry S., Lattanzi Riccardo, Sodickson Daniel K., Cloos Martijn A.. Hybrid-state free precession in nuclear magnetic resonance. *Communications Physics*. 2019;2(1):73.
- [27] Malik Shaihan J., Teixeira Rui P. A. G., West Daniel J., Wood Tobias C., Hajnal Joseph V.. Steady-state imaging with inhomogeneous magnetization transfer contrast using multiband radiofrequency pulses. *Magn. Reson. Med.*. 2020;83(3):935-949.
- [28] Uecker M., Hohage T., Block K. T., Frahm J.. Image reconstruction by regularized nonlinear inversion-joint estimation of coil sensitivities and image content. *Magn. Reson. Med.*. 2008;60(3):674–682.
- [29] Vasanawala S., Murphy M., Alley M., et al. Practical parallel imaging compressed sensing MRI: Summary of two years of experience in accelerating body MRI of pediatric patients. *Proc. IEEE Int. Symp. Biomed. Imaging*. 2011;:1039–1043.
- [30] Beck A., Teboulle M.. A Fast Iterative Shrinkage-Thresholding Algorithm for Linear Inverse Problems. *SIAM J. Img. Sci.*. 2009;2(1):183–202.
- [31] Uecker M., Virtue P., Ong F., et al. Software toolbox and programming library for compressed sensing and parallel imaging. In: ; 2013; Sedona.
- [32] Blumenthal Moritz, Luo Guanxiong, Schilling Martin, Holme H. Christian M., Uecker Martin. Deep, deep learning with BART. *Magnetic Resonance in Medicine*. 2023;89(2):678-693.
- [33] Dormand J.R., Prince P.J.. A family of embedded Runge-Kutta formulae. *Journal of Computational and Applied Mathematics*. 1980;6(1):19 - 26.

- [34] Schmitt Peter, Griswold Mark A, Jakob Peter M, et al. Inversion recovery TrueFISP: quantification of T1, T2, and spin density. *Magn. Reson. Med.*. 2004;51(4):661–667.
- [35] Wansapura Janaka P., Holland Scott K., Dunn R. Scott, Ball Jr. William S.. NMR relaxation times in the human brain at 3.0 tesla. *J. Magn. Reson. Imaging.* 1999;9(4):531-538.
- [36] Deimling M., Heid O.. Magnetization prepared trueFISP imaging. *Proceedings of the 2nd Annual Meeting of ISMRM, San Francisco.* 1994;:495.
- [37] Deshpande Vibhas S., Chung Yiu-Cho, Zhang Qiang, Shea Steven M., Li Debiao. Reduction of transient signal oscillations in true-FISP using a linear flip angle series magnetization preparation. *Magn. Reson. Med.*. 2003;49(1):151-157.
- [38] Chung Sohae, Kim Daniel, Breton Elodie, Axel Leon. Rapid B1+ mapping using a preconditioning RF pulse with TurboFLASH readout. *Magn. Reson. Med.*. 2010;64(2):439-446.
- [39] Wang Xiaoqing, Rosenzweig Sebastian, Scholand Nick, Holme H Christian M, Uecker Martin. Model-based Reconstruction for Simultaneous Multi-slice T1 Mapping using Single-shot Inversion-recovery Radial FLASH. *Magn. Reson. Med.*. 2021;85:1258–1271.
- [40] Wang Xiaoqing, Uecker Martin. *Data for: Model-Based Reconstruction for Simultaneous Multi-Slice T1 Mapping using Single-Shot Inversion-Recovery Radial FLASH.* 2020.
- [41] Sumpf T. J., Petrovic A., Uecker M., Knoll F., Frahm J.. Fast T2 Mapping With Improved Accuracy Using Undersampled Spin-Echo MRI and Model-Based Reconstructions With a Generating Function. *IEEE Trans. Med. Imaging.* 2014;33(12):2213–2222.
- [42] Stupic Karl F., Ainslie Maureen, Boss Michael A., et al. A standard system phantom for magnetic resonance imaging. *Magn. Reson. Med.*. 2021;86(3):1194-1211.
- [43] Deichmann Ralf. Fast high-resolution T1 mapping of the human brain. *Magn. Reson. Med.*. 2005;54(1):20–27.
- [44] Uecker M., Lai P., Murphy M. J., et al. ESPIRiT—an eigenvalue approach to autocalibrating parallel MRI: where SENSE meets GRAPPA. *Magn. Reson. Med.*. 2014;71(3):990–1001.
- [45] Bieri O., Scheffler K.. On the origin of apparent low tissue signals in balanced SSFP. *Magn. Reson. Med.*. 2006;56(5):1067-1074.
- [46] Graham S. J., Henkelman R. Mark. Understanding pulsed magnetization transfer. *J. Magn. Reson. Imaging.* 1997;7(5):903-912.

- [47] Maier Oliver, Schoormans Jasper, Schloegl Matthias, et al. Rapid T1 quantification from high resolution 3D data with model-based reconstruction. *Magn. Reson. Med.*. 2019;81(3):2072–2089.
- [48] Tan Zhengguo, Hohage Thorsten, Kalentev Olkesandr, et al. An eigenvalue approach for the automatic scaling of unknowns in model-based reconstructions: Applications to real-time phase-contrast flow MRI. *NMR Biomed.*. 2017;30:e3835.
- [49] Assländer Jakob, Lattanzi Riccardo, Sodickson Daniel K., Cloos Martijn A.. Optimized quantification of spin relaxation times in the hybrid state. *Magn. Reson. Med.*. 2019;82(4):1385-1397.
- [50] Feng Li, Liu Fang, Soultanidis Georgios, et al. Magnetization-prepared GRASP MRI for rapid 3D T1 mapping and fat/water-separated T1 mapping. *Magn. Reson. Med.*. 2021;.
- [51] Look David C, Locker Donald R. Time saving in measurement of NMR and EPR relaxation times. *Rev. Sci. Instrum.*. 1970;41(2):250–251.
- [52] Deichmann R, Haase A. Quantification of T1 values by SNAPSHOT-FLASH NMR imaging. *Journal of Magnetic Resonance (1969)*. 1992;96(3):608–612.
- [53] Roeloffs Volkert, Wang Xiaoping, Sumpf Tilman J., Untenberger Markus, Voit Dirk, Frahm Jens. Model-based reconstruction for T1 mapping using single-shot inversion-recovery radial FLASH. *Int. J. Imag. Syst. Tech.*. 2016;26(4):254-263.
- [54] Clare Stuart, Jezzard Peter. Rapid T1 mapping using multislice echo planar imaging. *Magn. Reson. Med.*. 2001;45(4):630-634.
- [55] Scheffler K., Lehnhardt S.. Principles and applications of balanced SSFP techniques. *Eur. Radiol.*. 2003;13(11):2409–2418.
- [56] Ehses Philipp, Seiberlich Nicole, Ma Dan, et al. IR TrueFISP with a golden-ratio-based radial readout: Fast quantification of T1, T2, and proton density. *Magn. Reson. Med.*. 2013;69(1):71-81.
- [57] Pfister Julian, Blaimer Martin, Kullmann Walter H., Bartsch Andreas J., Jakob Peter M., Breuer Felix A.. Simultaneous T1 and T2 measurements using inversion recovery TrueFISP with principle component-based reconstruction, off-resonance correction, and multicomponent analysis. *Magn. Reson. Med.*. 2019;81(6):3488-3502.

List of Figures **Figure 1** Illustration of the operators used in the Bloch model-based reconstruction. The bottom part presents the ODEs for the signal and the derivatives.

Figure 2 Left: Temporal evolution of the partial derivatives with respect to R_1 , R_2 and B_1 estimated for an IR bSSFP sequence with the SAB, DQ with varying perturbation levels h and the analytical references. **Right:** Plot with point-wise errors of the various DQ methods and the SAB with respect to the analytical reference. Note that the errors are presented in ppm for visualization.

Figure 3 A: The slice-selection gradient based simulation for a Hamming-windowed sinc-shaped inversion pulse simulated with the RK54 framework is shown (left). The point-wise errors of the RK54 (top), the STM technique (center) and the ROT method (bottom) with sampling rate 1 MHz are plotted for the x-, y- and z- component of the magnetization. Note that the errors are scaled by large factors for visualization. **B:** The runtime of the STM technique is compared to the reference RK54 method and a ROT simulation performed with a sampling rate of 1 MHz. The simulation is performed for 101 isochromats homogeneously distributed along a slice-selection gradient during a FLASH sequence for various numbers of repetitions. The maximum of 1000 is chosen to cover about 4 s of acquisition, required to measure enough data points for mapping high T_1 values. A more detailed version of this figure has been added to the Supplementary Section S3.

Figure 4 Reconstructed T_1 parameter maps for radial single-shot IR FLASH data acquired from a numerical (**A**) and measured phantom (**B**) as well as a human brain (**C**). The Bloch model-based reconstruction and the differences between the two methods are shown in the middle. The difference map is scaled up by a factor of 20 to improve visualization. On the right the T_1 values of the color-coded ROIs (arrows) of the Bloch reconstruction vs. Look-Locker reconstruction are plotted together with standard deviations. Besides the in vivo T_1 map presented in **C**, the Bloch model-based technique reconstructs a complex valued M_0 map, a relative flip angle map and complex coil sensitivities shown in **D**.

Figure 5 A: Reconstructed T_1 and T_2 parameter maps and the corresponding ROI values for numerical radial single-shot IR bSSFP data of a digital multi-coil reference object simulated in k-space. The left side shows the reconstructed parameter maps and the right the ROI analysis results in Bland-Altman plots relative to the simulated reference values. The analyzed ROIs are marked and numbered in the T_1 map.

B: Reconstructed T_1 and T_2 parameter maps and the corresponding ROI values for a radial single-shot IR bSSFP measurement of the T_2 spheres of the NIST system phantom. The left side corresponds to the rightmost ROI analysis. The right side presents the comparison of the analyzed ROIs reconstructed with the Bloch model-based technique for various signal model assumptions compared with gold-standard reference values in Bland-Altman plots. For improved visualization individual outliers are removed from the plot.

Figure 6 The T_1 parameter map reconstructed from a radial single-shot IR

FLASH in vivo dataset with a Look-Locker model-based reconstruction is shown on the left. It also shows the reconstructed T_1 parameter maps of a radial single-shot IR bSSFP in vivo dataset acquired on the same brain slice for short RF pulses (D_{RF} : 1 ms, TR: 4.88 ms) on the top and long RF pulses (D_{RF} : 2.5 ms, TR: 10.8 ms) on the bottom reconstructed with the Bloch model-based reconstruction. In the center column the difference maps are shown. The values corresponding to the colored ROIs are listed in Table 2. On the right the T_2 parameter maps for the short and long RF pulse experiments are shown reconstructed from the IR bSSFP sequence.

Figure S1 A: Reconstructed T_1 and T_2 parameter maps and the corresponding ROI values for numerical radial single-shot IR bSSFP data of a digital multi-coil reference object simulated in k-space. The left side shows the reconstructed parameter maps and the right the ROI analysis results relative to the simulated reference values with standard deviations. The analyzed ROIs are marked and numbered in the T_1 map. **B:** Reconstructed T_1 and T_2 parameter maps and the corresponding ROI values for a radial single-shot IR bSSFP measurement of the T_2 spheres of the NIST system phantom. The left side corresponds to the rightmost ROI analysis. The right side presents the comparison of the analyzed ROIs reconstructed with the Bloch model-based technique for various signal model assumptions compared with gold-standard reference values.

Figure S2 A: Reconstructed T_1 and T_2 parameter maps and all corresponding ROI values for simulated radial single-shot IR bSSFP data. Here, the datapoints removed to improve visualization in Figure 5 are included. Reconstructed parameter maps are shown on the left Bland-Altman plots using the simulated reference values are shown on the right. The ROIs are marked and numbered in the T_1 map. **B:** Reconstructed T_1 and T_2 parameter maps and the corresponding ROI values for a radial single-shot IR bSSFP measurement of the T_2 spheres of the NIST system phantom. The left side corresponds to the rightmost ROI analysis. The right side shows the Bland-Altman plots comparing the values of the ROIs reconstructed with the Bloch model-based technique for various assumptions used in the signal model compared with gold-standard reference values. For improved visualization individual outliers were removed from the plot.

Figure S3 A: T_1 maps reconstructed from single-shot IR FLASH (same as for Figure 4.B) for varying tolerance for computation of STMs. The forward model assumes on-resonant spins. The difference of the reconstructions for tolerances of $1e-5$ to $1e-2$ compared to the $1e-6$ reference are shown in the lower row. The differences are scaled by large factors for improved visualization.

B: Same analysis as for part A, but assuming a complex forward model including a slice-selection gradient.

C: Extension of Figure 3.A with varying tolerances for RK54 and STM and sampling rates for ROT.

D: Extension of Figure 3.B with varying tolerances for RK54 and STM as sampling rates for ROT.

Figure S4 Reconstructed T_1 parameter maps similar to Figure 4.B for varying wavelet regularization strengths β_0 for the Bloch model-based reconstruction.

tion (upper row). On the left a reference reconstruction estimated with the re-parameterized Look-Locker model-based technique is shown. In the bottom row the differences between Bloch model-based reconstruction and the reference map are shown scaled by a factor of 10 for improved visualization.

Figure S5 Visualization of the magnetization transfer effect in T_1 maps reconstructed from an IR bSSFP sequence with varying TR and T_{RF} . On the left the T_1 map corresponding to the longest $T_{RF} = 2.5$ ms is plotted with colored ROIs. The mean value of the relaxation parameter values for the colored areas is plotted with its standard deviation on the right for various length of RF-pulses T_{RF} . The dotted lines represent the fitted values following the analysis of section S5.

Figure S6 Bloch model-based reconstruction of the short RF pulse in vivo single-shot IR bSSFP dataset. The coil-sensitivities have been estimated with the regular method and have been added as fixed prior knowledge to both reconstruction. The top presents the regularized reconstruction, while the bottom results do not include any regularization on the parameter maps.

List of Tables **Table 1** Table listing the sequence parameters for the performed measurements of this work.

Table 2 Table listing the single-shot in-vivo IR bSSFP ROI analysis results presented in Figure 6.

Table S1 Table listing the fitting parameters estimated for Figure S5.

Table S2 Table listing the sequence parameters for the analysis in Figure S5.

A Combining Sensitivity Analysis with a Direct Sensitivity Analysis

The system matrix $A(t)$ in equation 10 can be extended to include the sensitivity analysis for the three partial derivatives R_1 , R_2 and B_1 :

$$A(t) = \begin{pmatrix} -R_2 & \gamma B_1(t) & -\gamma \sin(\phi(t))B_1(t)B_1(t) & 0 & 0 & 0 & 0 & 0 & 0 & 0 & 0 & 0 & 0 & 0 \\ -\gamma B_1(t) & -R_2 & \gamma \cos(\phi(t))B_1(t)B_1(t) & 0 & 0 & 0 & 0 & 0 & 0 & 0 & 0 & 0 & 0 & 0 \\ \gamma \sin(\phi(t))B_1(t)B_1(t) & -\gamma \cos(\phi(t))B_1(t)B_1(t) & -R_1 & 0 & 0 & 0 & 0 & 0 & 0 & 0 & 0 & 0 & 0 & M_0 R_1 \\ 0 & 0 & 0 & -R_2 & \gamma B_1(t) & -\gamma \sin(\phi(t))B_1(t)B_1(t) & 0 & 0 & 0 & 0 & 0 & 0 & 0 & 0 \\ 0 & 0 & 0 & -\gamma B_1(t) & -R_2 & \gamma \cos(\phi(t))B_1(t)B_1(t) & 0 & 0 & 0 & 0 & 0 & 0 & 0 & 0 \\ -1 & 0 & 0 & \gamma \sin(\phi(t))B_1(t)B_1(t) & -\gamma \cos(\phi(t))B_1(t)B_1(t) & -R_1 & 0 & 0 & 0 & 0 & 0 & 0 & 0 & M_0 \\ 0 & 0 & 0 & 0 & 0 & 0 & -R_2 & \gamma B_1(t) & -\gamma \sin(\phi(t))B_1(t)B_1(t) & 0 & 0 & 0 & 0 & 0 \\ 0 & -1 & 0 & 0 & 0 & 0 & -\gamma B_1(t) & -R_2 & \gamma \cos(\phi(t))B_1(t)B_1(t) & 0 & 0 & 0 & 0 & 0 \\ 0 & 0 & 0 & 0 & 0 & 0 & \gamma \sin(\phi(t))B_1(t)B_1(t) & -\gamma \cos(\phi(t))B_1(t)B_1(t) & -R_1 & 0 & 0 & 0 & 0 & 0 \\ 0 & 0 & -\gamma \sin(\phi(t))B_1(t) & 0 & 0 & 0 & 0 & 0 & 0 & -R_2 & \gamma B_1(t) & -\gamma \sin(\phi(t))B_1(t)B_1(t) & 0 & 0 \\ 0 & 0 & \gamma \cos(\phi(t))B_1(t) & 0 & 0 & 0 & 0 & 0 & 0 & -R_2 & -R_2 & \gamma \cos(\phi(t))B_1(t)B_1(t) & 0 & 0 \\ \gamma \sin(\phi(t))B_1(t) & -\gamma \cos(\phi(t))B_1(t) & 0 & 0 & 0 & 0 & 0 & 0 & 0 & \gamma \sin(\phi(t))B_1(t)B_1(t) & -\gamma \cos(\phi(t))B_1(t)B_1(t) & -R_1 & 0 & 0 \\ 0 & 0 & 0 & 0 & 0 & 0 & 0 & 0 & 0 & 0 & 0 & 0 & 0 & 0 \end{pmatrix}. \quad (22)$$

with its corresponding parameter vector from equation 9:

$$\mathbf{M}(t) \rightarrow \mathbf{x}(t) = \begin{pmatrix} M_x(t) \\ M_y(t) \\ M_z(t) \\ Z_{R_1,x}(t) \\ Z_{R_1,y}(t) \\ Z_{R_1,z}(t) \\ Z_{R_2,x}(t) \\ Z_{R_2,y}(t) \\ Z_{R_2,z}(t) \\ Z_{B_1,x}(t) \\ Z_{B_1,y}(t) \\ Z_{B_1,z}(t) \\ 1 \end{pmatrix}. \quad (23)$$

B Forward Model Derivatives

The derivative of \mathcal{A} in equation 19 follows by exploiting the Jacobi matrix and the product rule similar to [28, 13].

$$\mathbf{DA}(\mathbf{x}) \begin{pmatrix} dR_1 \\ dR_2 \\ dM_0 \\ dB_1 \\ dc_1 \\ \vdots \\ dc_N \end{pmatrix} = \begin{pmatrix} \mathcal{PF} \left(dc_1 M_{t_1} + c_1 \left[\frac{\partial M_{t_1}}{\partial R_1} dR_1 + \frac{\partial M_{t_1}}{\partial R_2} dR_2 + \frac{\partial M_{t_1}}{\partial M_0} dM_0 + \frac{\partial M_{t_1}}{\partial B_1} dB_1 \right] \right) \\ \vdots \\ \mathcal{PF} \left(dc_N M_{t_n} + c_N \left[\frac{\partial M_{t_n}}{\partial R_1} dR_1 + \frac{\partial M_{t_n}}{\partial R_2} dR_2 + \frac{\partial M_{t_n}}{\partial M_0} dM_0 + \frac{\partial M_{t_n}}{\partial B_1} dB_1 \right] \right) \\ \vdots \\ \mathcal{PF} \left(dc_N M_{t_n} + c_N \left[\frac{\partial M_{t_n}}{\partial R_1} dR_1 + \frac{\partial M_{t_n}}{\partial R_2} dR_2 + \frac{\partial M_{t_n}}{\partial M_0} dM_0 + \frac{\partial M_{t_n}}{\partial B_1} dB_1 \right] \right) \end{pmatrix}. \quad (24)$$

The adjoint of the derivative becomes

$$\mathbf{DA}^H(\mathbf{x}) \begin{pmatrix} y_{1,1} \\ y_{2,1} \\ \vdots \\ y_{n,N} \end{pmatrix} = \begin{pmatrix} dR_1 \\ dR_2 \\ dM_0 \\ dB_1 \\ dc_1 \\ \vdots \\ dc_N \end{pmatrix} = \begin{pmatrix} \sum_{j=1}^N \sum_{k=1}^n \overline{\left(\frac{\partial M_{t_k}}{\partial R_1} \right)} \cdot \bar{c}_j \cdot \mathcal{F}^{-1} [\mathcal{P}^H y_{k,j}] \\ \sum_{j=1}^N \sum_{k=1}^n \overline{\left(\frac{\partial M_{t_k}}{\partial R_2} \right)} \cdot \bar{c}_j \cdot \mathcal{F}^{-1} [\mathcal{P}^H y_{k,j}] \\ \sum_{j=1}^N \sum_{k=1}^n \overline{\left(\frac{\partial M_{t_k}}{\partial M_0} \right)} \cdot \bar{c}_j \cdot \mathcal{F}^{-1} [\mathcal{P}^H y_{k,j}] \\ \sum_{j=1}^N \sum_{k=1}^n \overline{\left(\frac{\partial M_{t_k}}{\partial B_1} \right)} \cdot \bar{c}_j \cdot \mathcal{F}^{-1} [\mathcal{P}^H y_{k,j}] \\ \sum_{k=1}^n \overline{M_{t_k}} \cdot \mathcal{F}^{-1} [\mathcal{P}^H y_{k,1}] \\ \vdots \\ \sum_{k=1}^n \overline{M_{t_k}} \cdot \mathcal{F}^{-1} [\mathcal{P}^H y_{k,N}] \end{pmatrix}. \quad (25)$$

C Look-Locker Reparameterization

The Look-Locker model represents a special solution of the Bloch equations for an IR FLASH sequence [51]. It assumes a perfect inversion, a small flip angle and short repetition times compared to the relaxation effects. Initial relaxation effects between the inversion and the first echo can be compensated analytically [43]. The original formulation of the Look-Locker model with the parameters M_0 , M_{ss} and R_1^* is

$$M_z(M_{ss}, M_0, R_1^*, t) = M_{ss} - (M_{ss} + M_0) \cdot e^{-R_1^* \cdot t} . \quad (26)$$

These parameters are related to the underlying physical parameters M_0 , R_1 and α_{eff} . With the assumption of short repetition times [52]

$$\frac{M_0}{M_{ss}} = \frac{R_1^*}{R_1} \quad (27)$$

the effective relaxation rate

$$R_1^* = R_1 + R'_1 = R_1 - \frac{1}{\text{TR}} \ln \cos \alpha_{\text{eff}} \quad (28)$$

splits into R_1 and the readout relaxation rate R'_1 determined by the effective flip angle α_{eff} [53]. The reparameterized Look-Locker model can be formulated as

$$M_z(M_0, R_1, R'_1, t) = M_0 \cdot \left(\frac{R_1}{R_1 + R'_1} - \left(1 + \frac{R_1}{R_1 + R'_1} \right) \cdot e^{-(R_1 + R'_1)t} \right) . \quad (29)$$

Here, Equation 29 depends directly on the physical parameters M_0 , R_1 and $R'_1 = -\frac{1}{\text{TR}} \ln \cos \alpha_{\text{eff}}$ and allows adding prior knowledge about smooth B1 maps [54, 43] to the reconstruction [53]. This reparameterized model can be directly compared to a Bloch model-based reconstruction using the same set of parameters.

D Scaling Factors

The output of the forward operator \mathcal{B} in equation 19 is the strength of the signal estimated by the Bloch simulation and its partial derivatives. The strength of the signal depends on the sequence and especially the applied flip angle. Therefore, the signals output differs for classical FLASH or bSSFP sequences influencing the weighting between the data fidelity and regularization terms changing the optimization behaviour.

A generic reconstruction aims for robustness against variations of the sequence parameters. It requires a scaling of the signal and its partial derivatives simulated within \mathcal{B} . The implemented scaling is motivated by the Look-Locker model assumption that the longitudinal magnetization M_z in equation 29 is proportional to the measured signal M_{xy} and scaled to 1. Thus, the signal of a simulation with an initial magnetization of length 1 requires scaling of the simulated signal output M_{xy} by the applied flip angle α and the relaxation effect $e^{-\frac{t_{\text{TE}}}{T_2}}$ during the echo time interval Δt_{TE} :

$$M_z = \frac{e^{-\frac{\Delta t_{\text{TE}}}{T_2}}}{\sin \alpha} \cdot M_{xy} . \quad (30)$$

Because of the short echo times of the sequences used in this work, the T_2 relaxation effect can be neglected. This assumption avoids additional T_2 dependencies of the estimated derivatives. The final scaling factor $\frac{1}{\sin \alpha}$ increases the robustness of the forward operator \mathcal{B} in equation 19 to the choice of the applied flip angle in FLASH based sequences. For a bSSFP type sequence the flip angle in equation 30 needs to be halved to take its dynamics on the $\alpha/2$ cone into account [55].

E IR bSSFP Information Encoding

The IR bSSFP signal behaviour is described by a limited exponential growth similar to the IR FLASH sequence [34]. A single inversion recovery can encode information for estimating 3 parameters. While the IR FLASH sequence is sensitive to exactly 3 parameters, the IR bSSFP is also sensitive to T_2 , leading to 4 parameters in total. With a single limited exponential growth this additional parameter can not be encoded and two parameters need to be coupled. For bSSFP sequences the relaxation parameters T_1 and T_2 are coupled. Prior knowledge about B_1 can be used to decouple both relaxation parameters [34, 56, 57].

F Symbolic Derivatives of IR bSSFP

The analytical signal model for an IR bSSFP can be derived from the Bloch equations with the assumptions of hard RF pulses, a perfect inversion and an ideal $\alpha/2 - \text{TR}/2$ magnetization preparation.

The signal is modelled by [34]:

$$M(M_{ss}, M_0^*, R_1^*, t) = M_{ss} - (M_0^* + M_{ss}) \cdot e^{-R_1^* \cdot t} \quad (31)$$

with

$$\begin{aligned} R_1^* &= R_1 \cos^2 \left(\frac{\alpha}{2} \right) + R_2 \sin^2 \left(\frac{\alpha}{2} \right) \\ M_{ss} &= \frac{M_0(1 - E_1) \sin \alpha}{1 - (E_1 - E_2) \cos \alpha - E_1 E_2} \\ &= \frac{M_0 \sin \alpha}{\stackrel{\text{TR} \ll T_{1,2}}{\left(\frac{R_1}{R_2} + 1 \right) - \cos \alpha \cdot \left(\frac{R_2}{R_1} - 1 \right)}} \\ M_0^* &= M_o \sin \left(\frac{\alpha}{2} \right) \end{aligned} \quad (32)$$

for

$$E_{1/2} = e^{-R_{1/2} \cdot t} . \quad (33)$$

This can be reparameterized to the physical parameters R_1 , R_2 , M_0 and α :

$$M(R_1, R_2, M_0, \alpha, t) = \frac{M_0 \sin \alpha}{\frac{R_2}{R_1} + 1 - \cos \alpha \left(\frac{R_2}{R_1} - 1 \right)} \quad (34)$$

$$- \frac{M_0 \sin \alpha \cdot e^{-R_1 \cos^2 \left(\frac{\alpha}{2} \right) \cdot t - R_2 \sin^2 \left(\frac{\alpha}{2} \right) \cdot t}}{\frac{R_2}{R_1} + 1 - \cos \alpha \left(\frac{R_2}{R_1} - 1 \right)}$$

$$- M_0 \sin \left(\frac{\alpha}{2} \right) \cdot e^{-R_1 \cos^2 \left(\frac{\alpha}{2} \right) \cdot t - R_2 \sin^2 \left(\frac{\alpha}{2} \right) \cdot t}$$

with its symbolic derivatives:

$$\frac{\partial M(R_1, R_2, M_0, \alpha, t)}{\partial R_1} = -M_0 R_2 \sin \alpha \cdot (\cos \alpha - 1) \cdot \frac{1 - C(R_1, R_2, \alpha, t)}{B^2(R_1, R_2, \alpha)} \quad (35)$$

$$+ M_0 R_1 t \sin \alpha \cos \left(\frac{\alpha}{2} \right) \cdot \frac{C(R_1, R_2, \alpha, t)}{B(R_1, R_2, \alpha)}$$

$$+ M_0 t \sin \left(\frac{\alpha}{2} \right) \cos^2 \left(\frac{\alpha}{2} \right) \cdot C(R_1, R_2, \alpha, t)$$

$$\frac{\partial M(R_1, R_2, M_0, \alpha, t)}{\partial R_2} = M_0 R_1 \sin \alpha \cdot (\cos \alpha - 1) \cdot \frac{1 - C(R_1, R_2, \alpha, t)}{B^2(R_1, R_2, \alpha)} \quad (36)$$

$$+ M_0 R_1 t \sin \alpha \sin^2 \left(\frac{\alpha}{2} \right) \cdot \frac{C(R_1, R_2, \alpha, t)}{B(R_1, R_2, \alpha)}$$

$$+ M_0 t \sin^3 \left(\frac{\alpha}{2} \right) \cdot C(R_1, R_2, \alpha, t)$$

$$\frac{\partial M(R_1, R_2, M_0, \alpha, t)}{\partial \alpha} = \frac{M_0 R_1 \sin^2 \alpha (R_2 - R_1) \cdot (C(R_1, R_2, \alpha, t) - 1)}{B^2(R_1, R_2, \alpha)} \quad (37)$$

$$- \frac{M_0 R_1 \sin \alpha \cdot C(R_1, R_2, \alpha, t) t \sin \left(\frac{\alpha}{2} \right) \cos \left(\frac{\alpha}{2} \right) (R_1 - R_2)}{B(R_1, R_2, \alpha)}$$

$$- \frac{M_0 R_1 \cos \alpha \cdot (C(R_1, R_2, \alpha, t) - 1)}{B(R_1, R_2, \alpha)}$$

$$- \frac{M_0}{2} \cos \left(\frac{\alpha}{2} \right) \cdot C(R_1, R_2, \alpha, t)$$

$$- M_0 \sin^2 \left(\frac{\alpha}{2} \right) \cos \left(\frac{\alpha}{2} \right) (R_1 - R_2) \cdot C(R_1, R_2, \alpha, t) t$$

$$\frac{\partial M(R_1, R_2, \alpha, t)}{\partial M_0} = \frac{\sin \alpha}{\frac{R_2}{R_1} + 1 - \cos \alpha \left(\frac{R_2}{R_1} - 1 \right)} \quad (38)$$

$$- \frac{\sin \alpha \cdot e^{-R_1 \cos^2 \left(\frac{\alpha}{2} \right) \cdot t - R_2 \sin^2 \left(\frac{\alpha}{2} \right) \cdot t}}{\frac{R_2}{R_1} + 1 - \cos \alpha \left(\frac{R_2}{R_1} - 1 \right)}$$

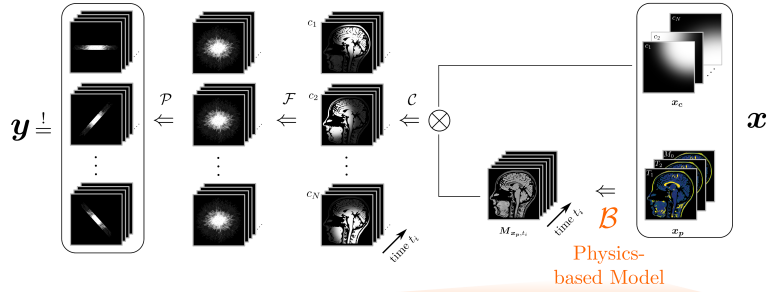
$$- \sin \left(\frac{\alpha}{2} \right) \cdot e^{-R_1 \cos^2 \left(\frac{\alpha}{2} \right) \cdot t - R_2 \sin^2 \left(\frac{\alpha}{2} \right) \cdot t}$$

with

$$B(R_1, R_2, \alpha) = (R_1 - R_2) \cos \alpha + R_1 + R_2 \quad (39)$$

$$C(R_1, R_2, \alpha, t) = \exp \left(-R_1 \cos^2 \left(\frac{\alpha}{2} \right) \cdot t - R_2 \sin^2 \left(\frac{\alpha}{2} \right) \cdot t \right) .$$

$$\hat{x} = \underset{\mathbf{x}_c, \mathbf{x}_p}{\operatorname{argmin}} (\|\mathbf{y} - \mathcal{PFC}(\mathbf{x}_c, \mathcal{B}(\mathbf{x}_p))\|_2^2 + \alpha \mathcal{Q}(\mathbf{x}_c) + \beta \mathcal{R}(\mathbf{x}_p))$$



Bloch ODE

$$\frac{d\mathbf{M}}{dt} = \begin{pmatrix} -R_2 & \gamma B_z & -\gamma \sin \phi B_1 & 0 \\ -\gamma B_z & -R_2 & \gamma \cos \phi B_1 & 0 \\ \gamma \sin \phi B_1 & -\gamma \cos \phi B_1 & -R_1 & R_1 M_0 \\ 0 & 0 & 0 & 0 \end{pmatrix} \begin{pmatrix} M_x \\ M_y \\ M_z \\ 1 \end{pmatrix}$$

Sensitivity ODE

$$\frac{d}{dt} \mathbf{Z} = \begin{pmatrix} 0 & -M_x & -\gamma \sin \phi M_z \\ 0 & -M_y & \gamma \cos \phi M_z \\ M_0 - M_z & 0 & \gamma(\sin \phi M_x - \cos \phi M_y) \end{pmatrix} + \begin{pmatrix} -R_2 & \gamma B_z & -\gamma \sin \phi B_1 \\ -\gamma B_z & -R_2 & \gamma \cos \phi B_1 \\ \gamma \sin \phi B_1 & -\gamma \cos \phi B_1 & -R_1 \end{pmatrix} \cdot \mathbf{Z}$$

Figure 1: Illustration of the operators used in the Bloch model-based reconstruction. The bottom part presents the ODEs for the signal and the derivatives.

Table 1: Table listing the sequence parameters for the performed measurements of this work.

Sequence	IR FLASH			IR bSSFP			Turbo FLASH			Spin-Echo	
	phantom	in vivo	phantom	in vivo	phantom	in vivo	phantom	in vivo	phantom	phantom	phantom
Object	4.B	4.C, 4.D, 6.B	5	6	5	6	5	6	5	5	5
Figure	4.1 1.84	4.1 2.58	4.88 2.44	4.88 2.44	2000 2.14	2000 2.14	2000 2.14	2000 2.14	8000 15	8000 (15:40:455)	
TR/TE [ms]	6	6	45	45	8	8	8	8	-	-	-
FA [°]	1	1	1	1	-	-	-	-	-	-	-
T_{RF} [ms]	5	5	5	5	5	5	5	5	5	5	5
Nominal Slice Thickness [mm]	1020	1000	1000	1000	1	1	1	1	1	1	1
Repetitions	20	20	20	20	20	20	20	20	20	20	20
Coils	4	4	4	4	-	-	-	-	-	-	-
BWTP	256	256	192	256	192	256	192	256	256	256	256
BR	192	200	200	200	200	200	200	200	200	200	200
FoV [mm]	0:04	0.04	0:05	0:05	0:04	0:04	0:04	0:04	34:16	34:16	34:16
Duration [min:s]	#tiny GA=7	#tiny GA=7	#tiny GA=7	#tiny GA=7	#tiny GA=7	#tiny GA=7	#tiny GA=7	#tiny GA=7	$T_{inv}=30:250:2530$ ms		
others											

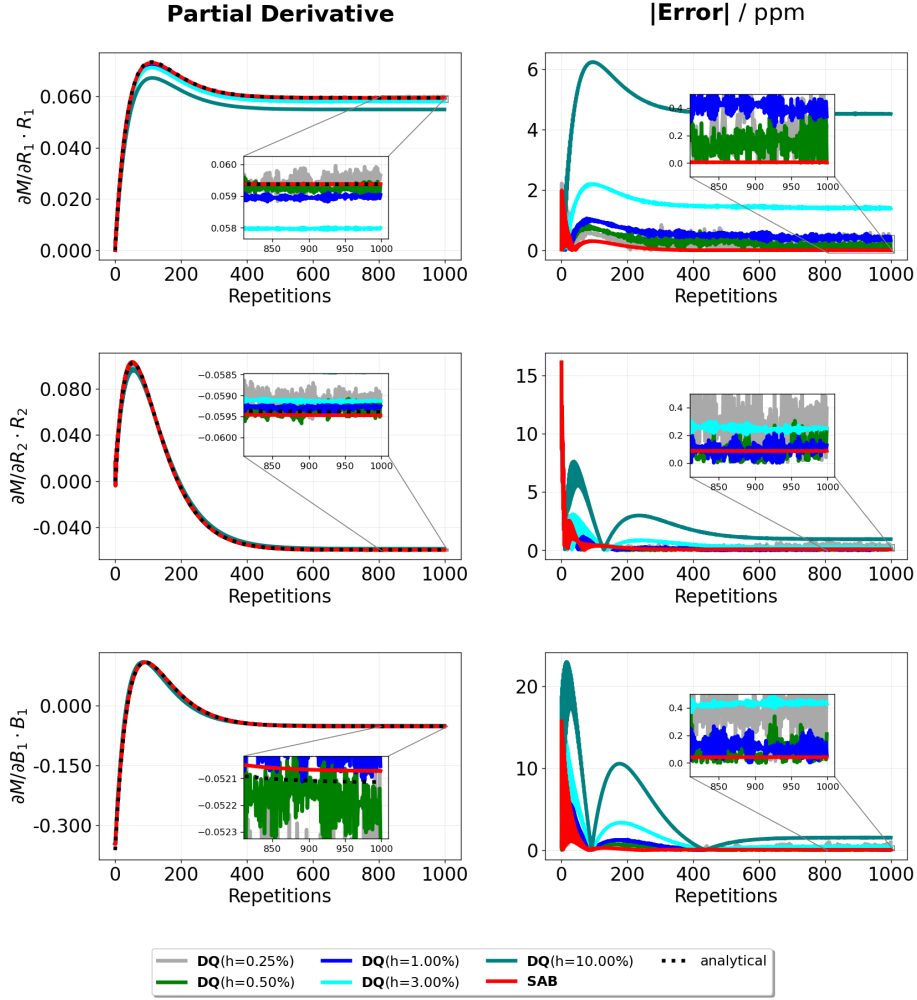


Figure 2: **Left:** Temporal evolution of the partial derivatives with respect to R_1 , R_2 and B_1 estimated for an IR bSSFP sequence with the SAB, DQ with varying perturbation levels h and the analytical references. **Right:** Plot with point-wise errors of the various DQ methods and the SAB with respect to the analytical reference. Note that the errors are presented in ppm for visualization.

Table 2: Table listing the single-shot in-vivo IR bSSFP ROI analysis results presented in Figure 6.

	$T_{1,IR \text{ FLASH}} [s]$	$T_{1,IR \text{ bSSFP, short}} [s]$	$T_{1,IR \text{ FLASH, long}} [s]$	$T_{2,IR \text{ bSSFP, short}} [s]$	$T_{2,IR \text{ bSSFP, long}} [s]$
ROI 1	0.737 ± 0.016	1.35 ± 0.019	1.061 ± 0.019	0.024 ± 0.001	0.033 ± 0.001
ROI 2	1.736 ± 0.299	2.434 ± 0.413	2.226 ± 0.456	0.066 ± 0.02	0.096 ± 0.088

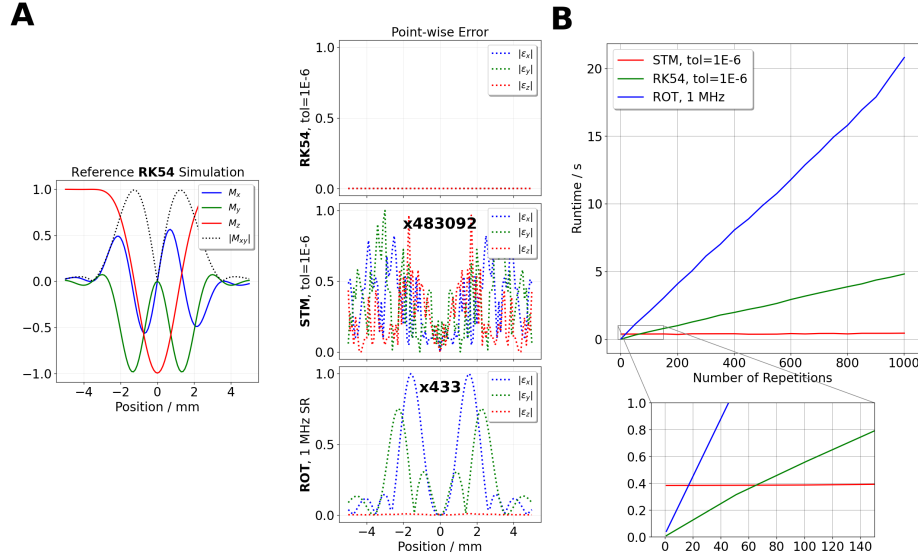


Figure 3: **A**: The slice-selection gradient based simulation for a Hamming-windowed sinc-shaped inversion pulse simulated with the RK54 framework is shown (left). The point-wise errors of the RK54 (top), the STM technique (center) and the ROT method (bottom) with sampling rate 1 MHz are plotted for the x-, y- and z- component of the magnetization. Note that the errors are scaled by large factors for visualization. **B**: The runtime of the STM technique is compared to the reference RK54 method and a ROT simulation performed with a sampling rate of 1 MHz. The simulation is performed for 101 isochromats homogeneously distributed along a slice-selection gradient during a FLASH sequence for various numbers of repetitions. The maximum of 1000 is chosen to cover about 4 s of acquisition, required to measure enough data points for mapping high T_1 values. A more detailed version of this figure has been added to the Supplementary Section S3.

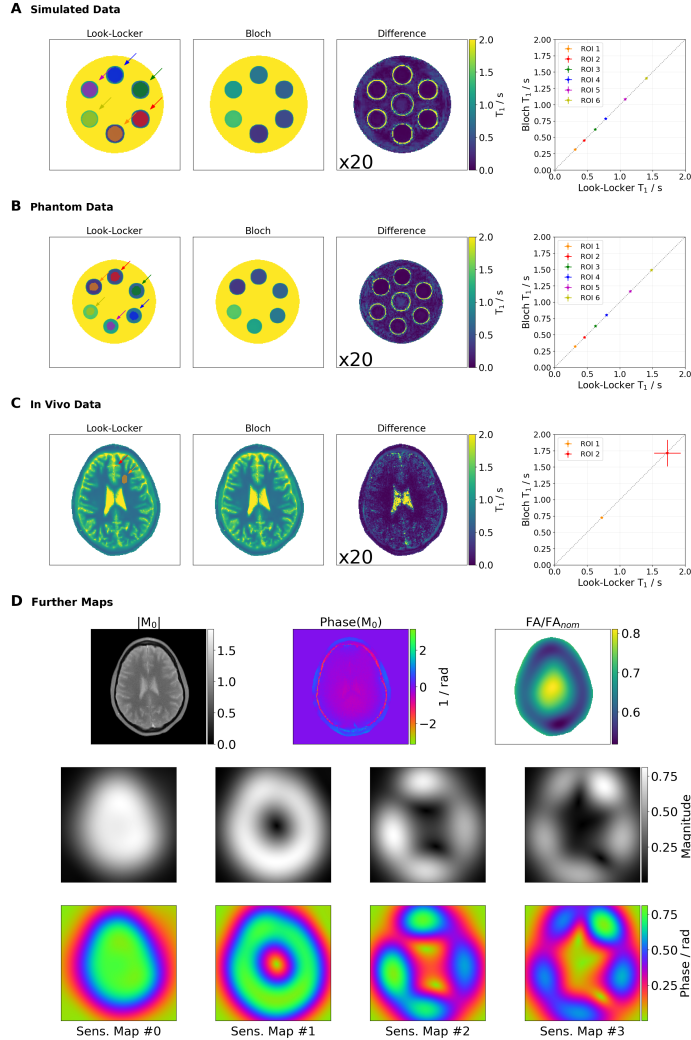


Figure 4: Reconstructed T_1 parameter maps for radial single-shot IR FLASH data acquired from a numerical (**A**) and measured phantom (**B**) as well as a human brain (**C**). The Bloch model-based reconstruction and the differences between the two methods are shown in the middle. The difference map is scaled up by a factor of 20 to improve visualization. On the right the T_1 values of the color-coded ROIs (arrows) of the Bloch reconstruction vs. Look-Locker reconstruction are plotted together with standard deviations. Besides the in vivo T_1 map presented in **C**, the Bloch model-based technique reconstructs a complex valued M_0 map, a relative flip angle map and complex coil sensitivities shown in **D**.

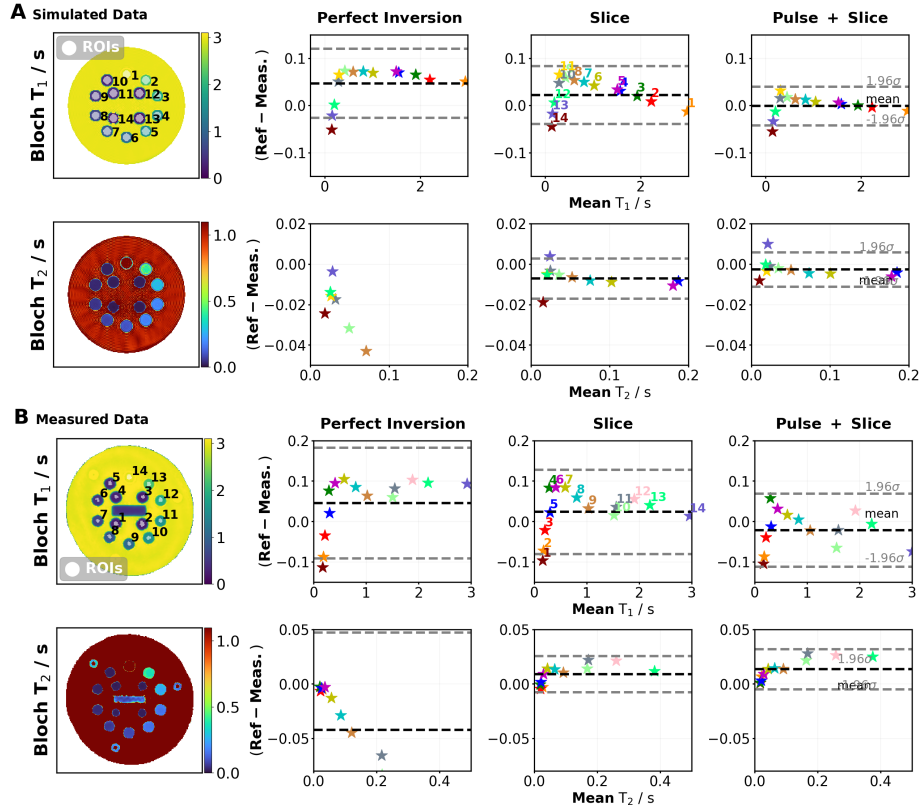


Figure 5: **A**: Reconstructed T_1 and T_2 parameter maps and the corresponding ROI values for numerical radial single-shot IR bSSFP data of a digital multi-coil reference object simulated in k-space. The left side shows the reconstructed parameter maps and the right the ROI analysis results in Bland-Altman plots relative to the simulated reference values. The analyzed ROIs are marked and numbered in the T_1 map. **B**: Reconstructed T_1 and T_2 parameter maps and the corresponding ROI values for a radial single-shot IR bSSFP measurement of the T_2 spheres of the NIST system phantom. The left side corresponds to the rightmost ROI analysis. The right side presents the comparison of the analyzed ROIs reconstructed with the Bloch model-based technique for various signal model assumptions compared with gold-standard reference values in Bland-Altman plots. For improved visualization individual outliers are removed from the plot.

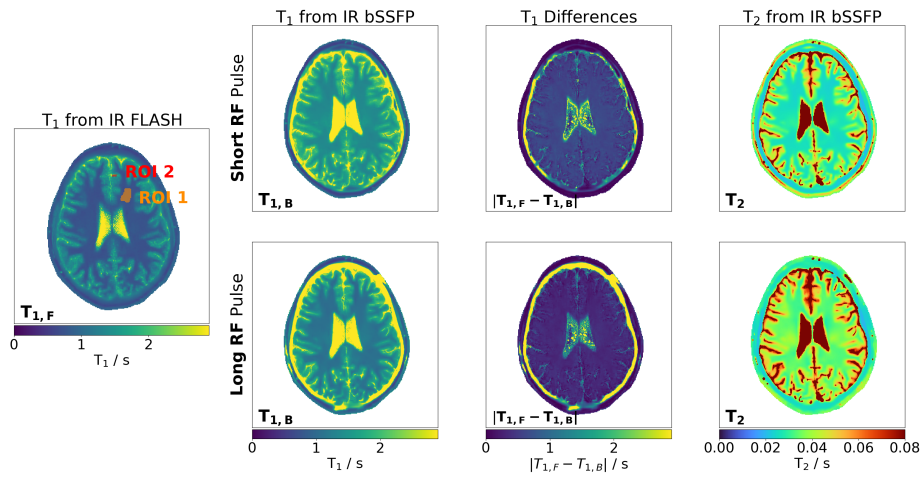


Figure 6: The T_1 parameter map reconstructed from a radial single-shot IR FLASH in vivo dataset with a Look-Locker model-based reconstruction is shown on the left. It also shows the reconstructed T_1 parameter maps of a radial single-shot IR bSSFP in vivo dataset acquired on the same brain slice for short RF pulses (D_{RF} : 1 ms, TR: 4.88 ms) on the top and long RF pulses (D_{RF} : 2.5 ms, TR: 10.8 ms) on the bottom reconstructed with the Bloch model-based reconstruction. In the center column the difference maps are shown. The values corresponding to the colored ROIs are listed in Table 2. On the right the T_2 parameter maps for the short and long RF pulse experiments are shown reconstructed from the IR bSSFP sequence.

Supporting Information

S1 Supporting Figure S1

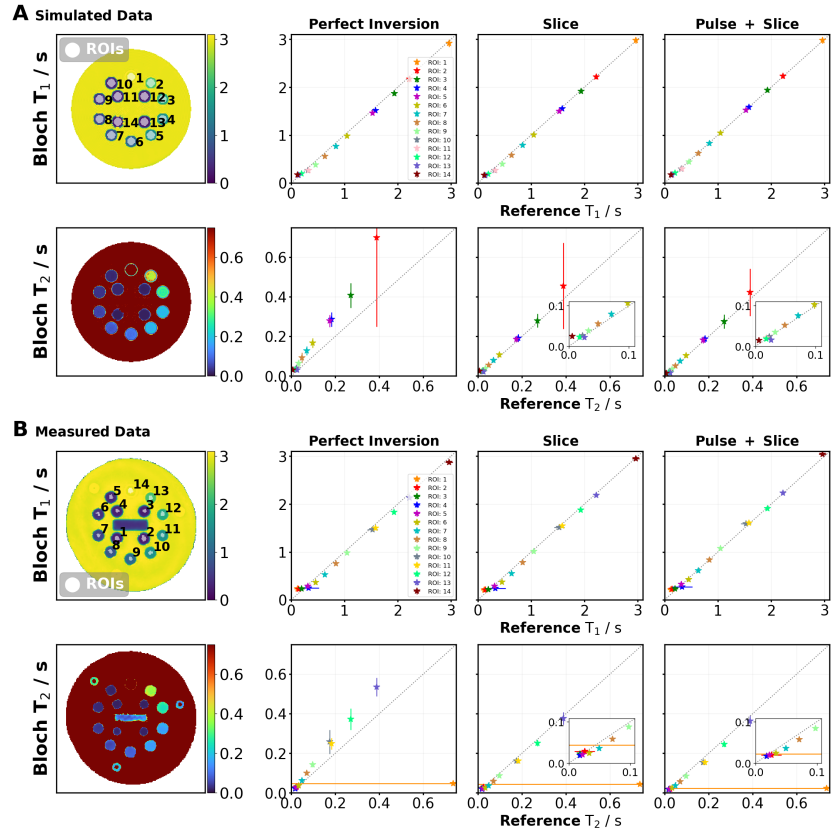


Figure S1: **A**: Reconstructed T_1 and T_2 parameter maps and the corresponding ROI values for numerical radial single-shot IR bSSFP data of a digital multi-coil reference object simulated in k-space. The left side shows the reconstructed parameter maps and the right the ROI analysis results relative to the simulated reference values with standard deviations. The analyzed ROIs are marked and numbered in the T_1 map. **B**: Reconstructed T_1 and T_2 parameter maps and the corresponding ROI values for a radial single-shot IR bSSFP measurement of the T_2 spheres of the NIST system phantom. The left side corresponds to the rightmost ROI analysis. The right side presents the comparison of the analyzed ROIs reconstructed with the Bloch model-based technique for various signal model assumptions compared with gold-standard reference values.

S2 Supporting Figure S2

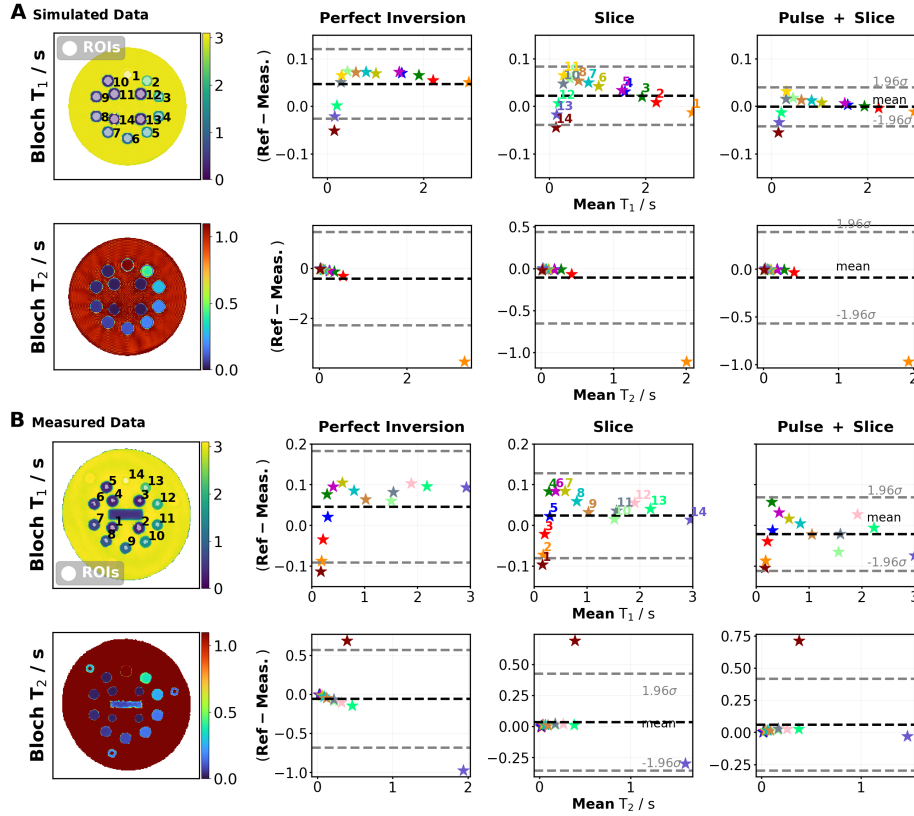


Figure S2: **A:** Reconstructed T_1 and T_2 parameter maps and all corresponding ROI values for simulated radial single-shot IR bSSFP data. Here, the datapoints removed to improve visualization in Figure 5 are included. Reconstructed parameter maps are shown on the left Bland-Altman plots using the simulated reference values are shown on the right. The ROIs are marked and numbered in the T_1 map. **B:** Reconstructed T_1 and T_2 parameter maps and the corresponding ROI values for a radial single-shot IR bSSFP measurement of the T_2 spheres of the NIST system phantom. The left side corresponds to the rightmost ROI analysis. The right side shows the Bland-Altman plots comparing the values of the ROIs reconstructed with the Bloch model-based technique for various assumptions used in the signal model compared with gold-standard reference values. For improved visualization individual outliers were removed from the plot.

S3 Supporting Figure S3: Simulation Accuracy

This section discusses the simulation accuracy of the ODE solvers for different tolerances and sampling rates in more detail. In Figure S3.A reconstructions of the IR FLASH phantom from Figure 4.B using the Bloch model-based reconstruction with signal model assumptions of only on-resonant spins and with spins distributed along a slice-selection gradient are shown. The reconstructions are performed with varying tolerance for the STM simulation method while keeping the initial step-size of the RK54 solver constant at $1\text{E-}4$.

For the on-resonance results the difference maps are small. Here, the reconstructed parameter maps for higher error tolerances are very similar to the reference map. For the signal model with simulation of the slice-selection gradient the reconstructed parameter maps are similar up to a tolerance of 0.001, while lower values result in large variations in the T_1 parameter map. The important result is, that the error of the simulation from an STM tolerance value of 0.001 still allows for accurate reconstructions even for complex spin dynamics.

In Figure S3.B the error plot from Figure 3 is extended to include more values for tolerance and sampling rate. To translate the required STM tolerance of 0.001 from Figure S3.A for complex dynamics to the required sampling rate for the ROT simulation, it demonstrates the point-wise errors (PWE) for RK54, STM and ROT for the same simulation with slice-selection gradient. The tolerance value for the estimated limit of STM of 0.001 produces an error similar to the 1 MHz sampling rate. This leads to the conclusion that at least a sampling rate of 1 MHz is required for accurate reconstruction of complex spin dynamics involving slice-selection gradients.

The simulation times for the same analysis with slice-selection gradient as presented in Figure 3 are shown in S3.C for multiple solver tolerances and sampling rates.

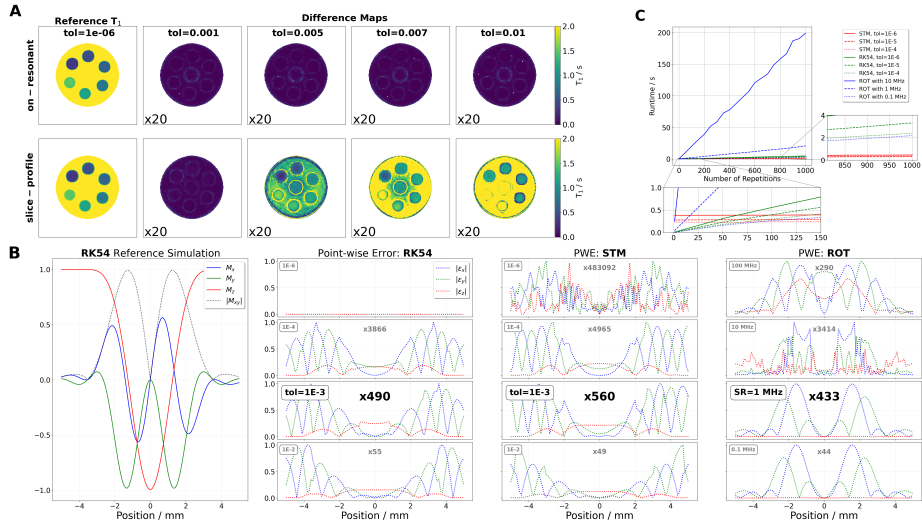


Figure S3: **A:** T_1 maps reconstructed from single-shot IR FLASH (same as for Figure 4.B) for varying tolerance for computation of STMs. The forward model assumes on-resonant spins. The difference of the reconstructions for tolerances of 1e-5 to 1e-2 compared to the 1e-6 reference are shown in the lower row. The differences are scaled by large factors for improved visualization. **B:** Same analysis as for part A, but assuming a complex forward model including a slice-selection gradient. **C:** Extension of Figure 3.A with varying tolerances for RK54 and STM and sampling rates for ROT. **D:** Extension of Figure 3.B with varying tolerances for RK54 and STM as sampling rates for ROT.

S4 Supporting Figure S4

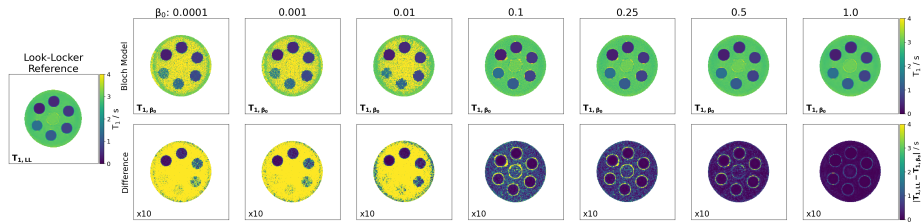


Figure S4: Reconstructed T_1 parameter maps similar to Figure 4.B for varying wavelet regularization strengths β_0 for the Bloch model-based reconstruction (upper row). On the left a reference reconstruction estimated with the reparameterized Look-Locker model-based technique is shown. In the bottom row the differences between Bloch model-based reconstruction and the reference map are shown scaled by a factor of 10 for improved visualization.

S5 Supporting Figure S5: Influence of the Magnetization Transfer Effect

To get an estimate of the magnetization transfer effect (MT) influence on the reconstructed T_1 parameter maps, multiple single-shot IR bSSFP experiments were performed with varying TR and T_{RF} . The sequence parameters are shown in Table S2. The analytical representation of the signal behaviour during an IR bSSFP experiment can be described by the equation F10. Following [56] the MT effect reduces the T_1^* as well as the steady-state magnetization M_{ss} , while not affecting M_0 . They propose an exponential model for correction of the effect of MT on M_{ss} :

$$M_{ss}(\beta) = (M_{ss}^{\text{no MT}} - M_{ss}^{\text{full MT}}) \cdot (1 - e^{-k \cdot \beta}) + M_{ss}^{\text{full MT}} \quad (40)$$

Here, the signal which is not affected by MT is denoted as $M_{ss}^{\text{no MT}}$, the signal from a fully-saturated solid pool is $M_{ss}^{\text{full MT}}$, the rate constant is k and the increase in RF pulse duration is β .

The T_1 value for an IR bSSFP can be estimated by

$$T_1 = \frac{T_1^*}{M_{ss}} M_0 \cos\left(\frac{\alpha}{2}\right) \quad (41)$$

with the flip angle α .

Taking into account that T_1^* is less affected by MT than M_{ss} [56], we assume that the MT influence on T_1 follows the model:

$$T_1(\beta) \approx \frac{1}{(a - b) \cdot (1 - e^{-k' \cdot \beta}) + b} \quad (42)$$

Equation 42 is fitted to the different relaxation parameters from various acquisitions with different TR and T_{RF} (Figure S5).

The estimated parameters a , b and k' have no direct physical interpretation, but can be used to interpolate an MT-free T_1 for $\beta \rightarrow \infty$. The parameters of the fit are shown in Table S1.

The results for $T_1(\beta \rightarrow \infty)$ suggest that the MT effect plays a significant role in the T_1 offset observed in Figure 6, but also indicates that it might not explain the complete discrepancy.

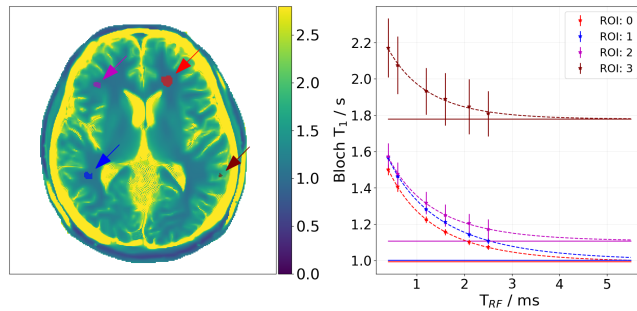


Figure S5: Visualization of the magnetization transfer effect in T_1 maps reconstructed from an IR bSSFP sequence with varying TR and T_{RF} . On the left the T_1 map corresponding to the longest $T_{RF} = 2.5$ ms is plotted with colored ROIs. The mean value of the relaxation parameter values for the colored areas is plotted with its standard deviation on the right for various length of RF-pulses T_{RF} . The dotted lines represent the fitted values following the analysis of section S5.

S6 Supporting Figure S6

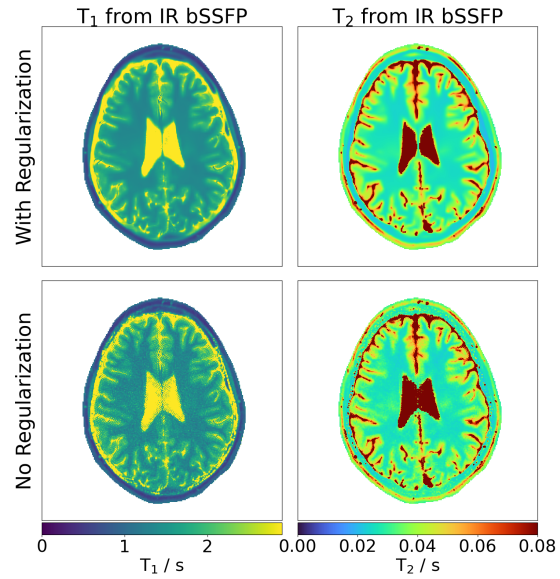


Figure S6: Bloch model-based reconstruction of the short RF pulse in vivo single-shot IR bSSFP dataset. The coil-sensitivities have been estimated with the regular method and have been added as fixed prior knowledge to both reconstruction. The top presents the regularized reconstruction, while the bottom results do not include any regularization on the parameter maps.

S7 Supporting Table S1

Table S1: Table listing the fitting parameters estimated for Figure S5.

	a [s]	b [s]	k' [s]
ROI 1	0.931 ± 0.006	0.510 ± 0.003	0.723 ± 0.023
ROI 2	0.923 ± 0.013	0.498 ± 0.005	0.620 ± 0.041
ROI 3	0.834 ± 0.01	0.498 ± 0.006	0.786 ± 0.059
ROI 4	0.519 ± 0.007	0.382 ± 0.008	0.992 ± 0.158

S8 Supporting Table S2

Table S2: Table listing the sequence parameters for the analysis in Figure S5.

Sequence	IR bSSFP	IR bSSFP	IR bSSFP	IR bSSFP	IR bSSFP	IR bSSFP	IR bSSFP
	in vivo	in vivo	in vivo	in vivo	in vivo	in vivo	in vivo
Object							
TR TE [ms]	3.8 1.9	4.0 2.0	4.6 2.3	5 2.5	5.5 2.75	6.14 3.07	
FA [°]	35	35	35	35	35	35	
T_{RF} [ms]	0.4	0.6	1.2	1.6	2.1	2.5	
Nominal Slice Thickness [mm]	5	5	5	5	5	5	
Repetitions	1000	1000	1000	1000	1000	1000	
Coils	20	20	20	20	20	20	
BWTP	1	1	1	1	1	1	
BR	256	256	256	256	256	256	
FoV [mm]	200	200	200	200	200	200	
Duration [min:s]	0:04	0:04	0:05	0:05	0:06	0:06	
others	#tiny GA=13	#tiny GA=13	#tiny GA=13	#tiny GA=13	#tiny GA=14	#tiny GA=13	#tiny GA=13